Cold Regions Science and Technology 239 (2025) 104591

Contents lists available at ScienceDirect

Cold Regions Science and Technology

journal homepage: www.elsevier.com/locate/coldregions

Simulating sea ice freezing using a continuum mechanical multi-phase and multi-component homogenization framework

Raghav Pathak [a], Seyed Morteza Seyedpour [a,b,*], Bernd Kutschan [c], Andrea Thom [a], Silke Thoms [c], Tim Ricken [a,b,*]

[a] Institute of Structural Mechanics and Dynamics in Aerospace Engineering, University of Stuttgart, Pfaffenwaldring 27, Stuttgart, 70569, Germany
[b] Porous Media Lab, Institute of Structural Mechanics and Dynamics in Aerospace Engineering, Faculty of Aerospace Engineering and Geodesy, University of Stuttgart, Pfaffenwaldring 27, Stuttgart, 70569, Germany
[c] Ecological Chemistry, Alfred Wegener Institute, Am Handelshafen 12, Bremerhaven, 27570, Germany

ARTICLE INFO

Keywords:
Sea ice
Climate change
Multifield problems
Extended theory of Porous Media (eTPM)

ABSTRACT

The formation of porous sea ice in the polar oceans is a complex process influenced by the interaction between saline seawater and temperature. As ocean warming and environmental changes continue in these regions, a likely impact on the microstructure of sea ice is expected to occur, which in turn affects the biogeochemical processes associated with ice formation. To better understand and model the phase transition phenomena, this study presents a biphasic model that considers both solid ice and saline seawater within the framework of extended Theory of Porous Media (eTPM). This approach applies a continuum mechanical treatment on multiple phases and components associated with ice and seawater. The model captures phase transition between ice and brine using an interfacial mass transfer method, where the mass exchange is treated as a jump across an interface separating the two phases. This mass production is governed by factors such as heat flux, specific enthalpies, and the interfacial area. The resulting system of equations provides a high-fidelity representation of the ice-brine interactions and is solved using the Finite Element Method (FEM). To validate the approach, the study includes academic test cases as proof of concept.

1. Introduction

Sea ice plays a crucial role in regulating the global climate, expanding and retreating in the polar regions each year. Since satellite monitoring began, the Arctic and Antarctic have shown distinct trends. However, despite regional differences, sea ice as a whole is highly dynamic and interacts with multiple coupled physical and biogeochemical processes (Paul et al., 2023). Changes in temperature, ocean currents, and atmospheric conditions affect its formation, growth, and melt cycles. Additionally, biogeochemical processes, such as ice algal growth, photosynthesis, and carbonate chemistry, are closely linked to the physical structure of the ice. These small-scale processes are not yet well integrated into large-scale models due to the lack of suitable parameterizations. While significant research efforts have focused on understanding the large-scale behavior of sea ice, there remains a substantial gap in knowledge regarding small-scale interactions.

In recent years, increasing attention has been given to incorporating small-scale physical-biogeochemical (P-BGC) processes into sea ice models. Since these processes are closely connected to the porous microstructure of sea ice, improving our understanding of this microstructure is crucial for accurately predicting future changes in sea ice cover. The physical and mechanical properties of sea ice as a macroscale continuum are a consequence of several small-scale processes associated with ice albedo, salinity, and temperature, cf. Vancoppenolle and Tedesco (2017), Tedesco and Vichi (2014), Worster and Rees Jones (2015), Eicken (1992). Hence, it becomes important to couple these processes with the phase transformation between saline seawater and solid ice at the interface between ocean and atmosphere. Several studies exist in the literature aimed at modeling individual small and large scale behavior. On the smaller scales, Morawetz et al. (2017), Kutschan et al. (2014, 2010, 2016), Lieblappen et al. (2018), Heorton et al. (2017) have presented modeling frameworks to study formation of dendritic patterns, microscale brine channels and frazil to polynas ice growth. The dimensions of temporal and spatial discretization are often in ranges of seconds and millimeters in these models. Large scale models (Åström et al., 2023; Streffing et al., 2022; Hunke et al., 2017; Danilov et al., 2015) often resolve the temporal and spatial

* Corresponding authors at: Institute of Structural Mechanics and Dynamics in Aerospace Engineering, University of Stuttgart, Pfaffenwaldring 27, Stuttgart, 70569, Germany.
E-mail addresses: seyed-morteza.seyedpour@isd.uni-stuttgart.de (S.M. Seyedpour), tim.ricken@isd.uni-stuttgart.de (T. Ricken).

https://doi.org/10.1016/j.coldregions.2025.104591
Received 12 February 2025; Received in revised form 29 April 2025; Accepted 23 June 2025
Available online 19 July 2025

dimensions in hours or days and kilometers, respectively. The primary focus of these models have been large scale sea ice drift behavior, and sea ice growth and decay modeling in terms of area. Small to large scale coupling has been gaining traction recently in the sea ice community. Weiss and Dansereau (2017) discussed linking scale in sea ice mechanics in the context of stress and deformation behavior including anisotropy, spatial localization and intermittency. Fu et al. (2021) studied multiscale variation characteristics of the three major Arctic sea ice drift patterns. However, the significant temporal periods were 1, 2, 4, and 8 years. The particle and the continuum systems have also been coupled to facilitate an effective representation of the dynamical and statistical features of sea ice across different scales (Deng et al., 2024). However, these studies are still in an early stage and no general consensus on significant coupling variables and behaviors can be found. A comprehensive numerical model of the deformable sea ice microstructure including the coupling of all relevant physical processes within the ice aims to bring insights into the small-scale processes such as salinity-temperature evolution (Notz and Worster, 2009; Notz, 2005; Griewank and Notz, 2013), brine channel and microscale dendritic pattern formation (Kutschan et al., 2014, 2010; Morawetz et al., 2017), among others.

The formation through freezing of sea ice is a complex and dynamic process. Once the surface water reaches its freezing point, ice crystals begin to form. These ice crystals initially appear as a slushy mixture of ice and water known as frazil ice. Frazil ice consists of small, needle-like ice crystals that are suspended in the water (McFarlane et al., 2015). These crystals can consolidate and stick together due to various factors, including wave action, turbulence, and wind. This process results in the formation of pancake ice, see Fig. 1, which consists of circular or irregularly shaped ice floes with raised edges. Pancake ice can continue to grow and merge to form a continuous ice cover and thickens over time. The frazil-pancake cycle shows the temporal evolution of sea ice, wherein frazil ice crystals aggregate and coalesce into pancake ice floes through a sequence of nucleation, aggregation, and consolidation processes driven by turbulent mixing and wave-induced motion (Doble, 2009; Nose et al., 2021; McDonald, 2018). Other types of interactions between ice and ocean water also exist, such as polynas, columnar, and rafted ice. Polynyas, localized areas of open water amidst sea ice, exert profound impacts on regional climate and ice dynamics, facilitating heat transfer and driving atmospheric and oceanic circulation patterns. Columnar ice, characterized by vertically aligned crystal structures resulting from the slow freezing of seawater, exhibits enhanced mechanical strength and thermal insulation properties compared to other ice types (Weeks and Ackley, 1986). Rafted ice formations, arising from the convergence and compression of ice floes, manifest as complex arrangements of overlapping ice layers, reflecting the interplay of mechanical forces and thermodynamic processes within the ice pack (Babko et al., 2002). As the seawater freezes, salt gets trapped between the pores of the ice forming interstitial liquid brine inclusions. With a decreasing temperature, more and more salt gets concentrated and during periods of warming, fresh ice dissolves with liquid brine, hence, expanding these brine channels. This gives rise to various salinity profiles as given in Eicken (1992). Studying the dynamics of these diverse range of phenomena associated with sea ice is pivotal for advancing our understanding of polar environments and global climate systems (Leppäranta, 2009).

The Theory of Porous Media (TPM) offers some key potential advantages to model complex porous materials like sea ice. First of all, TPM provides a well-established method to model deformable porous materials (Ehlers, 2002). TPM has also been found suitable to model complex phase transition phenomena in porous materials for biological (Lambers, 2023; Suditsch et al., 2021), geological (Thom, 2022), (Seyedpour et al., 2019a), and environmental mechanics (Ricken and Bluhm, 2010a; Schwarz et al., 2020), among others. TPM also provides a flexible framework to couple other multiphysical phenoma, like formation of dendrites using phase field solidification model on the microscale (Henning et al., 2016; Moj, 2017). Nutrient concentrations and solute diffusion processes have also been coupled with TPM (Seyedpour et al., 2019b). TPM has shown its utility also in the context of multi-phase modeling of ice formation process also (Bluhm et al., 2014; Schwarz et al., 2020; Pathak et al., 2024, 2025).

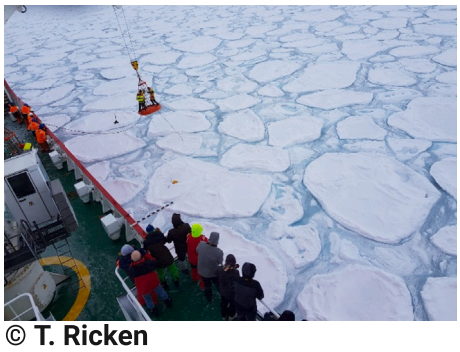

Fig. 1. Sea ice photographed during an Antarctic Expedition on St. Agulhas in 2017.

Thus, in this paper a modeling approach for the phase transition implemented to the extended Theory of Porous Media (eTPM) is presented, which includes not only the multi-phase, but also a multi-component description of the porous sea ice microstructure, as the individual immiscible phases of ice and liquid can be a mixture themselves. A phenomenological description of freezing of ice is presented. For this first modeling approach, a constant pore size with interconnected pores is assumed. The pores are then homogenized over the control volume and the liquid fraction is utilized as a measure of pore characteristic. A system of coupled partial differential equations (PDEs) is used which models the formation of ice in seawater. The Finite Element Method (FEM) is then applied to discretize and solve the system of equations.

2. Theoretical basis - extended Theory of Porous Media

The Theory of Porous Media (TPM) (Ehlers, 2002), which originates from the mixture theory (Bowen, 1976) with consideration of the concept of volume fractions, is widely used theory today for the description and study of the thermodynamic behavior of fully or partially saturated porous media, cf. (Ehlers, 2014). Through the use of volume fractions, it is possible to study the microstructure of complex heterogeneous materials. As will be discussed later, the microstructure is represented by means of spatial distribution of volume fractions, along with interactions between phases and evolution laws. This enables the macroscopic TPM equations to include effects due to microscopic structure and geometry without needing explicit resolution of each phase's geometry. Therefore, TPM has been found to be particularly suitable for multi-phase and multi-component materials, cf. (De Boer, 1996; De Boer and Ehlers, 1988), (Ricken, 2002; Ricken and de Boer, 2003; Ricken and Bluhm, 2010b; Ricken et al., 2014), (Moj et al., 2017), and (Bluhm et al., 2014).

The extended Theory of Porous Media (eTPM) as presented in Ricken et al. (2014, 2020) provides an approach to treat miscible substances φ^{β} present in the immiscible macro phases φ^{α}, see also (Seyedpour et al., 2023). The complex mixture body φ consists of κ macroscopic phases denoted as φ^{α}, with $\alpha = 1, \dots, \kappa$. Moreover, each immiscible phase can be comprised by ν components $\varphi^{\alpha\beta}$ which are solved and carried in phase φ^{α}. The overall mixture body can subsequently be homogenized as

$$\varphi = \bigcup_{\alpha}^{\kappa} \varphi^{\alpha} := \bigcup_{\alpha}^{\kappa} \left(\bigcup_{\beta}^{\nu} \varphi^{\alpha\beta} \right). \tag{1}$$

In the present case, the mixture body represents the biphasic ice-seawater mixture with $\alpha = \mathbf{I}, \mathbf{L}$, where $\varphi^{\mathbf{I}}$ denotes the solid ice matrix

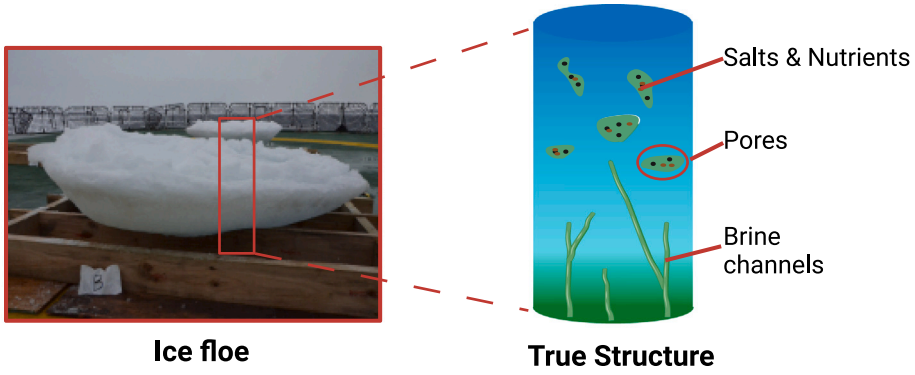

Fig. 2. Schematic of porous sea ice microstructure.

and φ^{L} the liquid brine. The brine phase consists of the miscible components $\varphi^{\mathrm{L}\beta}$ with $\{\beta = \mathrm{S}, w\}$, denoting the salt (s) and freshwater (w), respectively, see Fig. 2.

The concept of volume fractions is fundamental to describe the distribution of the different phases within a porous material. The continuum mechanical framework starts with the assumption of "smeared" continua to capture the heterogeneity and variability of the material. Smeared continua assume that these properties follow a statistical distribution. In the homogenized continuum all constituent phases are present in each point at all times and can be identified by their volume fraction. The liquids and/or gases present in the pores of the solid matrix can leave the mixture body.

The volume fraction n^{α} of a constituent is given as the local ratio of the volume element $\mathrm{d}v^{\alpha}$ of a given constituent φ^{α} with respect to the volume element $\mathrm{d}v$ of the overall medium with

$$\mathrm{n}^{\alpha} = \frac{\mathrm{d}v^{\alpha}}{\mathrm{d}v}. \tag{2}$$

Since the control volume is completely filled and leaves no vacant spaces, the saturation condition is given as

$$\sum_{\alpha} \mathrm{n}^{\alpha} = \mathrm{n}^{\mathbf{I}} + \mathrm{n}^{\mathbf{L}} = 1. \tag{3}$$

The total volume V and mass M of the mixture over the entire control volume can be written as the sum of all partial volumes V^{α} and masses M^{α} of the κ phases with

$$\mathrm{V} = \sum_{\alpha} \mathrm{V}^{\alpha} = \int_{\mathrm{B_I}} \sum_{\alpha} \mathrm{dv}^{\alpha} = \int_{\mathrm{B_I}} \sum_{\alpha} \mathrm{n}^{\alpha} \mathrm{dv} \tag{4}$$

$$\mathrm{M} = \sum_{\alpha} \rho^{\alpha}\ \mathrm{V} = \int_{\mathrm{B_I}} \sum_{\alpha} \rho^{\alpha} \mathrm{dv} = \int_{\mathrm{B_I}} \sum_{\alpha} \mathrm{n}^{\alpha} \rho^{\alpha \mathrm{R}}\, \mathrm{dv}.$$

The true density $\rho^{\alpha \mathrm{R}}$ is defined as the ratio of partial mass of the constituent dm^{α} to the partial volume dv^{α} with

$$\rho^{\alpha \mathrm{R}} = \frac{\mathrm{dm}^{\alpha}}{\mathrm{dv}^{\alpha}}. \tag{5}$$

The partial bulk density ρ^{α} of the constituent φ^{α} is defined as the product of its respective volume fraction n^{α} and macroscopic true density $\rho^{\alpha \mathrm{R}}$ with

$$\rho^{\alpha} = \frac{\mathrm{dm}^{\alpha}}{\mathrm{dv}} = \mathrm{n}^{\alpha} \rho^{\alpha \mathrm{R}}, \tag{6}$$

where $\rho^{\alpha \mathrm{R}}$ can also be written as a sum of real densities of the miscible components $\varphi^{\alpha\beta}$ with

$$\rho^{\alpha \mathrm{R}} = \sum_{\beta} \rho^{\alpha\beta}. \tag{7}$$

The partial pore densities are defined as

$$\rho^{\beta} = \frac{\mathrm{d}m^{\beta}}{\mathrm{dv}} = \frac{\mathrm{dv}^{\alpha}}{\mathrm{dv}} \frac{\mathrm{d}m^{\beta}}{\mathrm{dv}^{\alpha}} = \mathrm{n}^{\alpha} \rho^{\alpha\beta}. \tag{8}$$

Having a closer look to the seawater consisting of the miscible components fresh water and salt, see Fig. 3,

the previously defined Eqs. (7) and (8) are applied and lead to

$$\rho^{\beta} = \frac{\mathrm{dm}^{\beta}}{\mathrm{dv}} = \frac{\mathrm{dv}^{\mathbf{L}}}{\mathrm{dv}} \frac{\mathrm{dm}^{\beta}}{\mathrm{dv}^{\mathbf{L}}} = \mathrm{n}^{\mathbf{L}} \rho^{\mathrm{L}\beta} \tag{9}$$

with the real density of the liquid phase being the sum of the real densities of the miscible components $\rho^{\mathrm{L}\beta}$ with

$$\rho^{\mathrm{LR}} = \sum_{\beta} \rho^{\mathrm{L}\beta}. \tag{10}$$

Moreover, the mass fraction is given as the ratio of local mass of the solute to the sum of local masses of all solutes with

$$\mathrm{w}^{\mathrm{L}\beta} = \frac{\mathrm{dm}^{\beta}}{\sum_{\beta} \mathrm{dm}^{\beta}} = \frac{\rho^{\mathrm{L}\beta}}{\rho^{\mathbf{LR}}}. \tag{11}$$

Restrictions on exchange or production terms between the macroscopic phases have to be considered in terms of mass, momentum and energy. These are denoted by $\hat{\rho}^{\alpha}$, $\hat{\mathbf{p}}^{\alpha}$, and $\hat{\mathrm{e}}^{\alpha}$, respectively. According to Truesdell's metaphysical principles, cf. Truesdell (1984), the mixture body behaves as a single continua, constraining the sum of productions to zero, and hence, internal relations are given by

$$\sum_{\alpha} \hat{\rho}^{\alpha} = 0, \sum_{\alpha} \hat{\mathbf{p}}^{\alpha} \mathbf{o}, \sum_{\alpha} \hat{\mathrm{e}}^{\alpha} 0 \tag{12}$$

2.1. Kinematics

Considering the fundamental concept of the Theory of Porous Media that each constituent is present across the control volume at all time steps, the kinematics are governed by the concept of a superimposed continua. Each spatial point $\mathbf{x}$ in the actual configuration is simultaneously occupied by all constituents φ^{α}, and, in the extended TPM also by miscible components φ^{β}. The constituents and components are present in different reference positions at time t_0 and hence, a separate motion function χ^{α} and χ^{β}, respectively, is assigned to each particle, see Fig. 4.

Proceeding from that, the mass average velocity of the liquid brine $\mathbf{x}'_{\mathbf{L}}$ is defined as

$$\mathbf{x}'_{\mathbf{L}} = \frac{1}{\rho^{\mathbf{LR}}} \sum_{\beta} \rho^{\mathrm{L}\beta}\, \mathbf{x}'_{\mathrm{L}\beta} = \sum_{\beta} \mathrm{w}^{\mathrm{L}\beta} \mathbf{x}'_{\mathrm{L}\beta}, \tag{13}$$

which evolves from the different velocities of the components $\mathbf{x}'_{\mathrm{L}\beta}$ weighted by their mass fractions. The seepage velocity, an essential quantity in the TPM to describe advective liquid flow through a solid matrix is given for the present two-phase body with

$$\mathbf{w}_{\mathbf{LI}} = \mathbf{x}'_{\mathbf{L}} - \mathbf{x}'_{\mathbf{I}}. \tag{14}$$

The diffusion velocity in the framework of the eTPM is defined with

$$\mathbf{d}_{\beta \mathbf{L}} = \mathbf{w}_{\beta \mathbf{I}} - \mathbf{w}_{\mathbf{LI}}, \tag{15}$$

where $\mathbf{w}_{\beta \mathbf{I}}$ describes the difference velocity between component φ^{β} and the solid ice φ^{α}, and $\mathbf{w}_{\mathbf{LI}}$ the difference velocity between brine and ice.

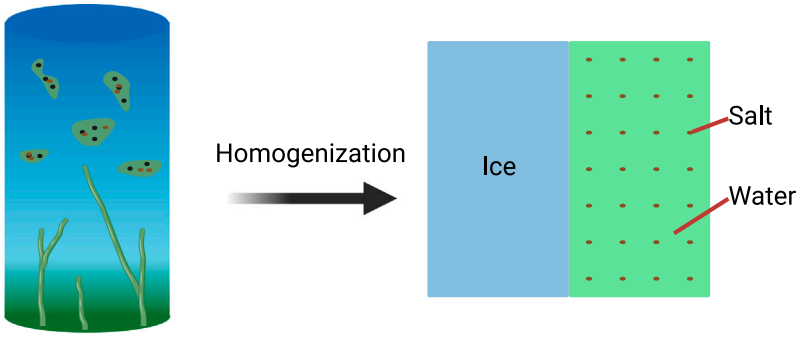

Fig. 3. Idealized representation of the seawater mixture.

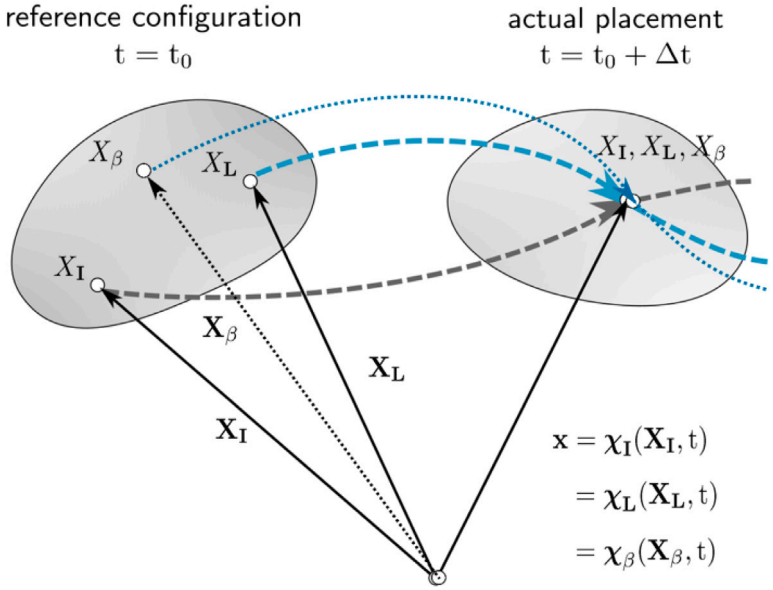

Fig. 4. Kinematics of a biphasic mixture with concentrations.

Further detailed derivation of the kinematics in the framework of the TPM involving coordinate transformation from Lagrangean to Eulerian, material time derivatives of field quantities, deformation and stress tensors of individual phases, among other quantities can be found in de Boer and Bluhm (1999).

2.2. Model set up for biphasic porous medium with salt concentration

The balance equations in the framework of the extended Theory of Porous Media (eTPM) are given by the local forms of the balance equations of mass, momentum, moment of momentum and energy of the constituents. These can be set up each for the macroscopic phase φ^α as well as for the component φ^β. The local forms are given in the aforementioned order with

$$(\rho^\alpha)'_\alpha + \rho^\alpha \operatorname{div} \mathbf{x}'_\alpha = \hat{\rho}^\alpha, \quad (\rho^\beta)'_\beta + \rho^\beta \operatorname{div} \mathbf{x}'_\beta = \hat{\rho}^\beta \tag{16}$$

$$\operatorname{div} \mathbf{T}^\alpha + \rho^\alpha(\mathbf{b} - \mathbf{x}''_\alpha) = \hat{\rho}^\alpha \mathbf{x}'_\alpha - \hat{\mathbf{p}}^\alpha, \quad \operatorname{div} \mathbf{T}^\beta + \rho^\beta(\mathbf{b} - \mathbf{x}''_\beta) = \hat{\rho}^\beta \mathbf{x}'_\beta - \hat{\mathbf{p}}^\beta, \tag{17}$$

$$\mathbf{T}^\alpha = (\mathbf{T}^\alpha)^T \tag{18}$$

$$\begin{aligned} \hat{\rho}^\alpha(\varepsilon^\alpha)'_\alpha - \mathbf{T}^\alpha \cdot \mathbf{D}_\alpha - \rho^\alpha r^\alpha + \operatorname{div} \mathbf{q}^\alpha &= \hat{e}^\alpha - \hat{\mathbf{p}}^\alpha \cdot \mathbf{x}'_\alpha - \hat{\rho}^\alpha(\varepsilon^\alpha - \frac{1}{2}\mathbf{x}'_\alpha \cdot \mathbf{x}'_\alpha), \\ \hat{\rho}^\beta(\varepsilon^\beta)'_\beta - \mathbf{T}^\beta \cdot \mathbf{D}_\beta - \rho^\beta r^\beta + \operatorname{div} \mathbf{q}^\beta &= \hat{e}^\beta - \hat{\mathbf{p}}^\beta \cdot \mathbf{x}'_\beta - \hat{\rho}^\beta(\varepsilon^\beta - \frac{1}{2}\mathbf{x}'_\beta \cdot \mathbf{x}'_\beta). \end{aligned} \tag{19}$$

In the equation for balance of momentum, $\mathbf{T}^\alpha$ and $\mathbf{b}$ are partial Cauchy stress tensors of the phase φ^α and the external body forces, respectively. $\mathbf{D}_\alpha$ is the symmetric part of the spatial velocity gradient $\mathbf{L} = (\mathbf{F}_\alpha)'_\alpha \mathbf{F}_\alpha^{-1}$ with the deformation gradient $\mathbf{F}_\alpha$. In the energy balance, ε^α, r^α and $\mathbf{q}^\alpha$ are the internal energy, external heat supply and the heat flux respectively. As defined in Eq. (12), $\hat{e}^\alpha$, $\hat{\mathbf{p}}^\alpha$ and $\hat{\rho}^\alpha$ are the local supply terms for energy, momentum and mass. All quantities are likewise defined for the component φ^β. A detailed derivations of all important quantities like pore densities in mass and molar units, material time derivatives of the immiscible phases and miscible constituents within them, motion functions, velocities, and advective and diffusive fluxes of the solute components within the framework of the extended Theory of Porous Media can be found in Thom (2022).

To provide thermodynamically consistent constitutive relations the entropy inequality is obtained. It is given in the local form with

$$\sum_\alpha [\rho^\alpha (\eta^\alpha)'_\alpha + \hat{\rho}^\alpha \eta^\alpha] \geq \sum_\alpha [\frac{1}{\theta^\alpha} \rho^\alpha r^\alpha - \operatorname{div}(\frac{1}{\theta^\alpha} \mathbf{q}^\alpha)] \tag{20}$$

where η^α is the specific entropy of the constituent φ^α.

2.2.1. Preliminary assumptions and field equations

Considering preliminary assumptions the governing equations for the model can be established. The mixture body is investigated with equal phase temperature with $\theta = \theta^\alpha$, so that the energy supply between the phases is equal to zero with $\hat{e}^\alpha = 0$. The solid ice matrix is assumed to be incompressible, but a density change can arise from temperature change, so that $\rho^{\mathrm{IR}} = \rho^{\mathrm{IR}}(\theta)$ is a function of temperature θ.

The same is valid for the liquid phase, however, the real density of can change through salinity change with $\rho^{\mathrm{LR}} = \rho^{\mathrm{LR}}(\mathrm{S}^{br})$. Mass exchange takes place between ice and liquid with $\hat{\rho}^{\mathbf{I}} = -\hat{\rho}^{\mathbf{L}}$. Thus, the mass balances for ice and liquid read

$$(\mathrm{n}^{\mathbf{I}})'_{\mathbf{I}}\,\rho^{\mathrm{IR}} + \mathrm{n}^{\mathbf{I}}(\rho^{\mathrm{IR}})'_{\mathbf{I}}\,\mathrm{div}\,\mathbf{x}'_{\mathbf{I}} = \hat{\rho}^{\mathbf{I}}, \quad (\mathrm{n}^{\mathbf{L}})'_{\mathbf{L}}\,\rho^{\mathrm{LR}} + \mathrm{n}^{\mathrm{L}}(\rho^{\mathrm{LR}})'_{\mathbf{L}}\,\mathrm{div}\,\mathbf{x}'_{\mathbf{L}} = -\hat{\rho}^{\mathbf{I}}. \quad (21)$$

Moreover, the mass conversation of salt with respect to the motion of ice is established with

$$\mathrm{n}^{\mathbf{L}}(\rho^{\mathrm{L}\beta})'_{\mathbf{I}} + (\mathrm{n}^{\mathbf{L}})'_{\mathbf{I}}\,\rho^{\mathrm{L}\beta}\mathrm{div}\,\mathrm{n}^{\mathbf{L}}\rho^{\mathrm{L}\beta}\,\mathbf{w}_{\beta\mathbf{I}} + \mathrm{n}^{\mathbf{L}}\rho^{\mathrm{L}\beta}\mathrm{div}\,\mathbf{x}'_{\mathbf{I}} = 0 \quad (22)$$

Use has been made of the reformulation of the material time derivative of an arbitrary quantity $(\cdot)$ w.r.t. the trajectory of the ice phase with $(\cdot)'_{\alpha} = (\cdot)'_{\mathbf{I}} + \mathrm{grad}(\cdot)\cdot\mathbf{w}_{\alpha\mathbf{I}}$ / $(\cdot)'_{\beta} = (\cdot)'_{\mathbf{I}} + \mathrm{grad}(\cdot)\cdot\mathbf{w}_{\beta\mathbf{I}}$. Evaluating the model under quasi-static conditions implies that $\mathbf{x}''_{\alpha} = 0$. Considering additionally the constraints given in Eq. (12) and Eq. (14), the local balances of momentum and their sum read

$$\begin{aligned} &\mathrm{div}\,\mathbf{T}^{\mathbf{I}} + \rho^{\mathbf{I}}\mathbf{b} = \hat{\rho}^{\mathbf{I}}\,\mathbf{x}'_{\mathbf{I}} - \hat{\mathbf{p}}^{\mathbf{I}}, \quad \mathrm{div}\,\mathbf{T}^{\mathbf{L}} + \rho^{\mathbf{L}}\mathbf{b} = -\hat{\rho}^{\mathbf{I}}\,\mathbf{x}'_{\mathbf{L}} + \hat{\mathbf{p}}^{\mathbf{I}},\\ &\mathrm{div}\,\mathbf{T} + \rho\mathbf{b} = -\hat{\rho}^{\mathbf{I}}\,\mathbf{w}_{\mathbf{LI}}, \end{aligned} \quad (23)$$

with $\mathbf{T} = \mathbf{T}^{\mathbf{I}} + \mathbf{T}^{\mathbf{L}}$ and $\rho = \rho^{\mathbf{I}} + \rho^{\mathbf{L}}$. The energy balance for the mixture reads by making use of the specific Helmholtz free energy $\psi^{\alpha} = \varepsilon^{\alpha} - \theta^{\alpha}\eta^{\alpha}$

$$\begin{aligned} &\sum_{\alpha}\{\rho^{\alpha}[(\psi^{\alpha})'_{\alpha} + (\theta)'_{\alpha}\eta^{\alpha} + \theta(\eta^{\alpha})'_{\alpha}] - \mathbf{T}^{\alpha}\cdot\mathbf{D}_{\alpha}\} + \mathrm{div}\,\mathbf{q} = \\ &- \hat{\mathbf{p}}^{\mathbf{L}}\cdot\mathbf{w}_{\mathbf{LI}} - \hat{\rho}^{\mathbf{I}}(\psi^{\mathbf{I}} - \psi^{\mathbf{L}} + \theta(\eta^{\mathbf{I}} - \eta^{\mathbf{L}})), \end{aligned} \quad (24)$$

with $\mathbf{q} = \mathbf{q}^{\mathbf{I}} + \mathbf{q}^{\mathbf{L}}$. Regarding the relation between components of the brine $\varphi^{\mathrm{L}\beta}$ and the overall mixture $\varphi^{\mathbf{L}}$,

$$\mathbf{T}^{\mathbf{L}} = \sum_{\beta}\mathbf{T}^{\mathrm{L}\beta}, \quad \eta^{\mathbf{L}} = \sum_{\beta}\eta^{\mathbf{L}\beta}, \quad \psi^{\mathbf{L}} = \sum_{\beta}\psi^{\mathrm{L}\beta} \quad (25)$$

2.2.2. Constitutive equations for sea ice-water mixture

For a thermodynamically consistent description, the entropy inequality is evaluated in a procedure according to Coleman and Noll (1963). As a common procedure in multi-phase material modeling, the material time derivative of the saturation condition in combination with the Lagrange multiplier λ is added to the inequality to serve as an additional constraint. For a more useful energy formulation the specific Helmholtz free energy ψ^{α} is implemented via $\psi^{\alpha} = \varepsilon^{\alpha} - \theta^{\alpha}\eta^{\alpha}$, so the local form of the entropy inequality yields

$$\begin{aligned} &\sum_{\alpha}\{-\rho^{\alpha}[(\psi^{\alpha})'_{\alpha} + (\theta)'_{\alpha}\eta^{\alpha}] + \mathbf{T}^{\alpha}\cdot\mathbf{D}_{\alpha} - \frac{1}{\theta}\,\mathrm{grad}\,\theta\cdot\mathbf{q}^{\alpha} - \hat{\rho}^{\alpha}(\psi^{\alpha} - \frac{1}{2}\,\mathbf{x}'_{\alpha}\cdot\mathbf{x}'_{\alpha})\\ &- \hat{\mathbf{p}}^{\alpha}\cdot\mathbf{x}'_{\alpha}\} + \lambda\{(1 - \sum_{\alpha}\mathrm{n}^{\alpha})'_{\mathbf{I}}\}. \geq 0 \end{aligned} \quad (26)$$

In the following, the square of the velocities connected with the mass exchange $\hat{\rho}^{\alpha}$ will be neglected as the problem is investigated under quasi-static conditions and velocities are assumed to be less than 1 m/s. To consider the multi-component description, a mass-specific Helmholtz free energy ψ^{β} is introduced, which yields after summing up over the components the Helmholtz energy $\psi^{\mathbf{L}}$ of the overall solution:

$$\rho^{\beta}\psi^{\beta} = \mathrm{n}^{\mathbf{L}}(\rho^{\mathrm{L}\beta}\psi^{\beta}) = \mathrm{n}^{\mathbf{L}}\psi^{\mathrm{L}\beta} \quad \text{with} \quad \sum_{\beta}\psi^{\mathrm{L}\beta} = \sum_{\beta}\rho^{\mathrm{L}\beta}\psi^{\beta} = \psi^{\mathbf{L}} \quad (27)$$

The evaluation of the final representation of the Clausius–Duhem entropy inequality provides energy conserving and dissipative constraints which have to be considered for the choice of potential functions (where we assume that the energy potentials exist and meet the restrictions obtained from the evaluation of the entropy inequality) $\psi^{\mathbf{I}}$ and $\psi^{\mathbf{L}}/\psi^{\beta}$, respectively:

- Energy conserving:

$$\begin{aligned} &\mathbf{T}^{\mathbf{I}} = -\mathrm{n}^{\mathbf{I}}\,\lambda\,(\frac{(\rho^{\mathrm{IR}})'_{\mathbf{I}}}{\rho^{\mathrm{IR}}})\,\mathbf{I} + \mathbf{T}^{\mathbf{I}}_{\mathrm{E}}, \quad \sum_{\beta}\mathbf{T}^{\beta} = \mathbf{T}^{\mathbf{L}} = -\mathrm{n}^{\mathbf{L}}\,\lambda\,\mathbf{I}\\ &\text{with} \quad \mathbf{T}^{\mathbf{I}}_{\mathrm{E}} = 2\,\rho^{\mathbf{I}}\,\mathbf{F}_{\mathbf{I}}\frac{\partial\psi^{\mathbf{I}}}{\partial\mathbf{C}_{\mathbf{I}}}\mathbf{F}^{\mathrm{T}}_{\mathbf{I}} \end{aligned} \quad (28)$$

$$\lambda = -\rho^{\mathbf{LR}}\,(\sum_{\beta}\frac{\partial\psi^{\mathrm{L}\beta}}{\partial\rho^{\mathrm{L}\beta}} + \frac{1}{\rho^{\mathrm{L}\beta}}\psi^{\mathrm{L}\beta}) \quad (29)$$

$$\eta^{\mathbf{I}} = -\frac{\partial\psi^{\mathbf{I}}}{\partial\theta}, \quad \eta^{\beta} = -\frac{1}{\rho^{\mathrm{L}\beta}}\frac{\partial\psi^{\mathrm{L}\beta}}{\partial\theta} \quad (30)$$

- Dissipative:

$$\begin{aligned} &\hat{\rho}^{\mathbf{I}} = -\delta_{\mu^{\mathbf{I}}}\,(\,\mu^{\mathbf{I}} - \mu^{\mathbf{L}}\,)\\ &\text{with} \quad \mu^{\mathbf{I}} = \psi^{\mathbf{I}} + \frac{\lambda}{\rho^{\mathrm{IR}}},\ \mu^{\mathbf{L}} = \psi^{\mathbf{L}} + \frac{\lambda}{\rho^{\mathbf{LR}}} \end{aligned} \quad (31)$$

$$\hat{\mathbf{p}}^{\beta} = \mathrm{w}^{\mathrm{L}\beta}\,\lambda\,\mathrm{grad}\,\mathrm{n}^{\mathbf{L}} + \hat{\mathbf{p}}^{\beta}_{\mathrm{E}}, \quad \hat{\mathbf{p}}^{\beta}_{\mathrm{E}} = -\delta_{\mathbf{w}_{\beta\mathbf{I}}}\mathbf{w}_{\beta\mathbf{I}} \quad (32)$$

$$\mathbf{q} = -\alpha_{\nabla\theta}\,\mathrm{grad}\,\theta \quad (33)$$

In the framework of various homogenization theories like the TPM (De Boer, 1996; Ehlers, 2002), mixture theory (MT) (Bowen, 1969; Passman, 1977; Drumheller, 1978), and local volume averaging theory (Hassanizadeh and Gray, 1979a,b; Lewis and Schrefler, 1999) from which the continuum mechanical models of porous materials are derived, the pores are assumed to be interconnected and have so far yielded satisfactory results for various fields of application. Starting from the fact that the pores are occupied by the fluid phase, the pore space property is incorporated using the volume fractions. It is then also possible to resolve the behavior of homogenized continuum body without knowing the actual size of each individual pore. The solid stress is a function of solid effective stress (or material law) and fluid pore pressure. The pore pressure is then determined using the volume fraction of solid $\mathrm{n}^{\mathbf{I}}$ (or $1 - \mathrm{n}^{\mathbf{L}}$) multiplied with the pore pressure $\mathrm{p}^{\mathbf{LR}}$. Eq. (28) provides the Cauchy stress relations $\mathbf{T}^{\mathbf{I}}$ and $\mathbf{T}^{\mathbf{L}}$ for the solid ice and brine. The split for $\mathbf{T}^{\mathbf{I}}$ follows the concept of effective stresses by Terzaghi (1943), which divides the total stresses into the effective part $\mathbf{T}^{\mathbf{I}}_{\mathrm{E}}$ covered by the soil matrix and the pore pressure part dependent on the Lagrange multiplier λ. The pore pressure part is also dependent on the density change $(\rho^{\mathrm{IR}})'_{\mathbf{I}}$. Related to the principle of effective stresses, λ is identified as the pore pressure $\mathrm{p}^{\mathbf{LR}}$. The constraint for the pressure (29) follows the derivation by Bowen (1967), which includes the definition for the chemical potential with $\mu^{\mathrm{L}\beta} = \partial\psi^{\mathrm{L}\beta}/\partial\rho^{\mathrm{L}\beta}$.

Besides changes in pressure due to hydraulic impacts, changes resulting from the variation of the chemical composition due to diffusion, osmosis or reaction can also be included in the model utilizing the chemical potential. Eq. (30) presents the common relation for the specific entropies, which are obtained by deriving the specific Helmholtz energy with respect the temperature. The dissipative parts include the correlations to mass exchange (31), interaction forces (32), and heat flux (33). Therein, again use has been made of the definition for the overall chemical potentials of solid ice and brine $\mu^{\mathbf{I}}$ and $\mu^{\mathbf{L}}$, see $(31)_2$. The parameters $\delta_{\mu^{\mathbf{I}}}$ and $\delta_{\mathbf{w}_{\beta\mathbf{I}}}$ are introduced as material parameters to comply with the dissipative inequality. More details on the restriction with reference to the mass supply can be found in Section 2.2.3.

By implementing the restriction for momentum exchange (32) into the momentum balance for component φ^{β}, a constitutive relation for the mass flux with respect to the solid ice can be derived, which constitutes of an advective ($\mathbf{w}_{\mathbf{LI}}$) and diffusive ($\mathbf{w}_{\beta\mathbf{L}}$) part with

$$\mathbf{j}^{\beta} = \mathrm{n}^{\mathbf{L}}\mathbf{j}^{\mathrm{L}\beta} = \mathrm{n}^{\mathbf{L}}\rho^{\mathrm{L}\beta}\mathbf{w}_{\beta\mathbf{I}} = \mathrm{n}^{\mathbf{L}}\rho^{\mathrm{L}\beta}\,(\mathbf{w}_{\mathbf{LI}} + \mathbf{w}_{\beta\mathbf{L}}). \quad (34)$$

Utilizing an approach for the material parameter $\delta_{\mathbf{w}_{\beta\mathbf{I}}}$ based on the approach presented in Thom (2022) with

$$\frac{(\mathrm{n}^{\mathbf{L}})^2}{\delta_{\mathbf{w}_{\beta\mathbf{I}}}} \overset{!}{=} \{\mathrm{d}^{\beta}_0 + \mathrm{k}^{\beta}_0\}, \quad (35)$$

where d^{β}_0 can be chosen as a pre-factor yielding *Fick*'s law of diffusion and k^{β}_0 a factor to derive a *Darcy* expression for the filter velocity $\mathrm{n}^{\mathbf{L}}\mathbf{w}_{\mathbf{LI}}$, the total mass flux formulation reads

$$\mathbf{j}^{\beta} = \mathrm{n}^{\mathbf{L}}\rho^{\mathbf{L}}\mathbf{w}_{\beta\mathbf{I}} = -\mathrm{n}^{\mathbf{L}}\mathrm{w}^{\mathrm{L}\beta}\mathrm{d}_{L\beta}\,\mathrm{grad}\,\mathrm{p}^{\mathbf{LR}} - \rho^{\mathrm{L}\beta}\frac{K^{\mathbf{I}}}{\eta^{\mathbf{LR}}}\mathrm{grad}\,\mathrm{p}^{\mathbf{LR}}. \quad (36)$$

Therein, $D_{L\beta}$ represents the diffusion coefficient of component φ^{β} in mixture $\varphi^{\mathbf{L}}$, $\mathrm{K}^{\mathbf{I}}$ is the intrinsic permeability and η^{LR} the dynamic viscosity of the mixture.

The restriction (33) for the heat flux vector $\mathbf{q}$ gained from the dissipation mechanism can directly be identified as Fourier's law (Fourier, 1822), which describes the heat conduction negative proportional to the temperature gradient with $\alpha_{\nabla\theta}$ as the head conduction coefficient.

To close the equation system, some more *ad hoc* assumptions are chosen regarding density and salinity. The bulk salinity of the ice-water mixture is given by the sum of salinities of ice and liquid multiplied by their respective volume fractions

$$\mathrm{S}^{\mathrm{bulk}} = \mathrm{n}^{\mathbf{I}}\,\mathrm{S}^{\mathrm{ice}} + \mathrm{n}^{\mathbf{L}}\,\mathrm{S}^{\mathrm{br}}. \tag{37}$$

It is also possible to reformulate the bulk salinity as a function of mass fractions using the relation $\mathrm{n}^{\alpha}\rho^{\alpha} = \mathrm{w}^{\alpha}$, yielding the relation with respect to mass fractions as $\mathrm{S}^{\mathrm{bulk}} = \mathrm{w}^{\mathbf{I}}\mathrm{S}^{\mathrm{ice}} + \mathrm{w}^{\mathbf{L}}\,\mathrm{S}^{\mathrm{br}}$. The liquid weight fraction includes both freshwater and salt constituents and is given as $\mathrm{w}^{\mathbf{L}} = \mathrm{w}^{\mathbf{L}s} + \mathrm{w}^{\mathbf{L}w}$ In physical terms, bulk salinity is the salinity of the water that is formed when a given sea-ice sample will be completely molten. In case that $\mathrm{w}^{\mathbf{L}}$ denotes the mass of the liquid brine and $\mathrm{w}^{\mathbf{I}}$ that of the solid pure ice, the bulk salinity is described by

$$\mathrm{S}^{\mathrm{bulk}} = \mathrm{w}^{\mathbf{L}s}/(\mathrm{w}^{\mathbf{L}} + \mathrm{w}^{\mathbf{I}}) \cdot 10^3 ppt, \tag{38}$$

whereas the brine salinity is defined as

$$\mathrm{S}^{\mathrm{br}} = \mathrm{w}^{\mathbf{L}s}/\mathrm{w}^{\mathbf{L}} \cdot 10^3 ppt. \tag{39}$$

With decreasing ice and brine temperatures, the Brine Volume Fraction (BVF) decreases and the ice becomes impermeable when BVF < 5% (Golden et al., 2007). Brine is then trapped in discrete pockets. Therein, liquid brine remains in thermodynamic equilibrium with the ice matrix whose temperature controls the brine volume and salinity. During ongoing cooling, brine pockets shrink as water freezes onto the walls of the pockets, thereby increasing the internal brine salinity. The increase of brine salinity due to the decrease in temperature is described by Notz and Worster (2009) as

$$\mathrm{S}^{\mathrm{br}} = -21.4\,\theta - 0.886\,\theta^2 - 0.0170\,\theta^3. \tag{40}$$

The situation is different however, in bottom ice, and also at the ice-seawater interface. In the open brine channel system, brine salinity might be still close to seawater salinity. Then, brine could become temporarily out of equilibrium with the ice matrix. It is also worth noting that several forms of the salinity-temperature Eq. (40) exist in literature. A comprehensive study of these can be found in Vancoppenolle et al. (2019) where the different equations are compared with each other. However, for the temperature range between $\theta = 0°C$ and $\theta = -22.9°C$, the equations yield comparable values till the hydrohalite precipitation discontinuity is reached. Another critical temperature value is $\theta = -8.2°C$ when the sodium sulfate starts precipitating, and hence the slope of the curve slightly changes. The error, however, is still less than 5% between the calculated salinity and data.

The real densities of ice ρ^{IR} and brine ρ^{LR} are dependent on the temperature and brine salinity, cf. (Petrich and Eicken, 2016)

$$\begin{aligned}\rho^{\mathrm{IR}} &= 917.0 - 0.1403\,\theta \\ \rho^{\mathrm{LR}} &= 1000.0 + 0.8\,\mathrm{S}^{\mathrm{br}}.\end{aligned} \tag{41}$$

2.2.3. Evolution equation for growing ice

The freezing process from sea water to ice is a complex procedure dependent on the concept of latent heat, which is the energy absorbed or released during a phase transition at constant temperature. A pure ice phase formed out of a brine mixture requires 334kJ/kg of latent heat release during the phase transition. The latent heat in the context of sea ice also depends on the temperature and salinity of the system by the factor $L(1+\frac{\mu S}{T})$, where $\mu = 0.054°C$ PSU^{-1} is the empirical constant, T is the temperature and S is the salinity of sea water. However, for temperature further away from freezing temperature $0°C$ these effects are quite small and can be neglected (Fang et al., 2022). Fig. 5 shows the latent heat transfer for phase transition between water and ice.

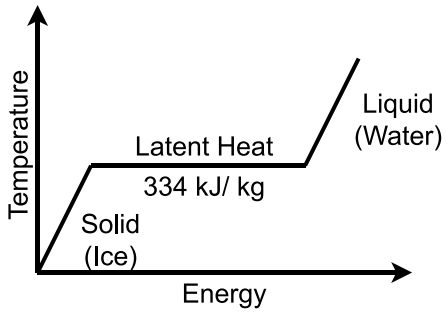

Fig. 5. Heat of fusion for freezing process.

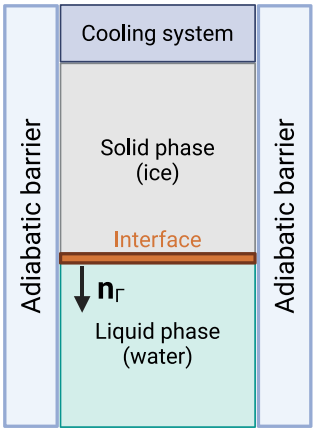

Fig. 6. Principle of 1D ice formation. *Source:* Taken from (Bluhm et al., 2014).

To transfer this phenomena to the TPM, an approach based on the physical motivation of an interface velocity between ice and water during a freezing process is used, see (Bluhm et al., 2014). Therein, the driving force of the velocity of the interface is equal to the difference of the heat flux vectors divided by the corresponding specific enthalpies h^{α}, see also Fig. 6. With the postulation of the pre-factor $\beta^{I}_{\psi^{IL}}$ the mass supply term finally reads according to Bluhm et al. (2014)

$$\beta^{I}_{\psi^{IL}} = \frac{\beta^{I}(\mathrm{div}\,\mathbf{q})_B}{(\Psi^{I} - \Psi^{L})(\mathrm{h}^{\mathbf{I}} - \mathrm{h}^{\mathbf{L}})} \quad \text{and} \quad \hat{\rho}^{\mathrm{I}} = -\frac{\beta^{I}(\mathrm{div}\,\mathbf{q})_B}{(\mathrm{h}^{\mathbf{I}} - \mathrm{h}^{\mathbf{L}})}. \tag{42}$$

A comparable ansatz is also introduced by Ehlers and Haeberle (2016), where the phase transition of water is described as a mass transfer across a singular surface which separates the available pore space into a disconnected part of water and ice. Proceeding from the implementation of jump conditions into the balance equations, an interfacial mass production term is derived. Transferred to the present problem, the growth term $\hat{\rho}^{\mathbf{I}}$ yields

$$\hat{\rho}^{\mathbf{I}} = a_{\Gamma}\frac{(\mathbf{q}^{\mathbf{L}} - \mathbf{q}^{\mathbf{I}}) \cdot \mathbf{n}_{\Gamma}}{(\mathrm{h}^{\mathbf{L}} - \mathrm{h}^{\mathbf{I}})}. \tag{43}$$

With this, the growth $\hat{\rho}^{\mathbf{I}}$ is dependent on the interfacial area a_{Γ}, the jump between the heat fluxes $\mathbf{q}^{\mathbf{L}}$ and $\mathbf{q}^{\mathbf{I}}$ and the specific enthalpies (latent heat) $\mathrm{h}^{\mathbf{L}}$ and $\mathrm{h}^{\mathbf{I}}$ of water and ice, respectively. The specific enthalpy can be derived from

$$h^{\beta} = \mu^{\beta} + \theta\,\eta^{\beta} = \psi^{\beta} + \frac{p^{L\beta}}{\rho^{L\beta}} + \theta\eta^{\beta}. \tag{44}$$

The interfacial area a_Γ is given as the quotient between the surface of the internal phase change referred to the overall volume with

$$a_\Gamma = \frac{\mathrm{d}a_\Gamma}{\mathrm{dv}}\,. \tag{45}$$

The interfacial area is assumed to be constant and acts a pre-factor in the thermodynamically motivated phenomenological growth term. The direction of the moving ice singular surface $\mathbf{n}_\Gamma$ is chosen to point in the direction of the temperature gradient.

3. Numerical treatment - Weak formulations

Taking into account the preliminary assumptions, constitutive relations and the saturation condition, the following quantities remain unknown:

$$\mathcal{R} = \mathcal{R}(\mathbf{x}, t) = \left\{\mathbf{u}_\mathrm{I}, \mathrm{n}^\mathbf{I}, \mathrm{S}^\mathrm{bulk}, \mathrm{p}^\mathrm{LR}, \theta\right\} \tag{46}$$

The weak formulations are derived following the standard Galerkin Finite Element Method (FEM) to determine the unknown field variables. The balance equations for the unknown quantities are multiplied with their respective test functions to get the final equations:

- Balance of momentum for mixture:

$$\int_{\mathrm{B_I}} (\sum_{\alpha}^{\mathrm{I,L}} \mathbf{T}^\alpha)\cdot \mathrm{grad}\,\delta\mathbf{u_I}\,\mathrm{dv} - \int_{\mathrm{B_I}} (\sum_{\alpha}^{\mathrm{I,L}} \rho^\alpha)\,\mathbf{b}\cdot\delta\mathbf{u_I}\,\mathrm{dv} = \int_{\partial\mathrm{B_I}} \{\mathbf{t}\cdot\delta\mathbf{u_I}\}\,\mathrm{da} \tag{47}$$

- Mass balance ice:

$$\int_{\mathrm{B_I}} \{(\mathrm{n}^\mathbf{I})'_\mathbf{I}\,\rho^\mathrm{IR} + \mathrm{n}^\mathbf{I}(\rho^\mathrm{IR})'_\mathbf{I}\,\mathrm{tr}\mathbf{D_I} - \hat{\rho}^\mathbf{I}\}\,\delta\mathrm{n}^\mathbf{I}\,\mathrm{dv} = 0 \tag{48}$$

- Concentration balance of salt:

$$\int_{\mathrm{B_I}} \{\mathrm{n}^\mathbf{L}(\mathrm{S}^\mathrm{br})'_\mathbf{I} + (\mathrm{n}^\mathbf{L})'_\mathbf{I}\,\mathrm{S}^\mathrm{br} + \frac{\mathrm{n}^\mathbf{L}}{\rho^\mathrm{LR}}\mathrm{S}^\mathrm{br}\,(\rho^\mathrm{LR})'_\mathbf{I} + \mathrm{n}^\mathbf{L}\,\mathrm{S}^\mathrm{br}\,\mathrm{tr}\mathbf{D_I}\}\,\delta\mathrm{S}^\mathrm{bulk}\,\mathrm{dv} \tag{49}$$

$$- \int_{\mathrm{B_I}} \{\frac{\mathbf{j}^\mathrm{Ls}}{\rho^\mathrm{LR}}\cdot\mathrm{grad}\,\delta\mathrm{S}^\mathrm{bulk}\}\,\mathrm{dv} = \int_{\partial\mathrm{B_I}} \{\frac{\mathbf{j}^\mathrm{Ls}}{\rho^\mathrm{LR}}\,\delta\mathrm{S}^\mathrm{bulk}\cdot\mathbf{n}\}\,\mathrm{da}$$

  where $\mathbf{j}^\mathrm{Ls} = \mathbf{j}^\mathrm{Ls}_\mathrm{adv} + \mathbf{j}^\mathrm{Ls}_\mathrm{diff}$ is the total salt flux consisting of advective and diffusive components.

- Mass balance for the mixture:

$$\int_{\mathrm{B_I}} -\{\mathrm{n}^\mathbf{L}\mathbf{w_{LI}}\cdot\mathrm{grad}\delta\mathrm{p}^\mathrm{LR}\}\,\mathrm{dv} + \int_{\mathrm{B_I}} \{\mathrm{tr}\,\mathbf{D_I} + \sum_\alpha \frac{\mathrm{n}^\alpha}{\rho^{\alpha\mathrm{R}}}(\rho^{\alpha\mathrm{R}})'_\mathbf{I} \tag{50}$$

$$- \hat{\rho}^\mathbf{I}(\frac{1}{\rho^\mathrm{LR}} - \frac{1}{\rho^\mathrm{IR}})\}\delta\mathrm{p}^\mathrm{LR}\,\mathrm{dv} = -\int_{\partial\mathrm{B_I}} \{\mathrm{n}^\mathbf{L}\mathbf{w_{LI}}\,\delta\mathrm{p}^\mathrm{LR}\cdot\mathbf{n}\}\,\mathrm{da}$$

- Energy balance for the mixture:

$$\int_{\mathrm{B_I}} \{\theta\rho^\mathbf{I}(\eta^\mathbf{I})'_\mathbf{I}\}\,\delta\theta\,\mathrm{dv} + \int_{\mathrm{B_I}} \{\theta\rho^\mathbf{L}(\eta^\mathbf{L})'_\mathbf{L}\}\,\delta\theta\,\mathrm{dv} - \int_{\mathrm{B_I}} \{\mathbf{q}\cdot\mathrm{grad}\,\delta\theta\}\,\mathrm{dv} \tag{51}$$

$$+ \int_{\mathrm{B_I}} \{\hat{\mathbf{p}}^\mathbf{I}_\mathrm{E}\cdot\mathbf{w_{LI}}\}\,\delta\theta\,\mathrm{dv} + \int_{\mathrm{B_I}} \{\hat{\rho}^\mathbf{I}\,[\mathrm{h}^\mathbf{L} - \mathrm{h}^\mathbf{I}]\}\,\delta\theta\,\mathrm{dv} = \int_{\partial\mathrm{B_I}} \{\mathbf{q}\,\delta\theta\cdot\mathbf{n}\}\,\mathrm{da}$$

Starting from (24), the energy equation is derived using the results of the evaluation of the entropy inequality as well as the mass balances for liquid and ice were included. Therein, the exchange term $\hat{\rho}^\mathbf{I}$ is connected with the heat of fusion for ice, where (44) is used. The weak formulations are discretized for the Finite Element Method (FEM) and implemented as a user element in the Finite Element Analysis Program (FEAP), cf. Taylor (2014).

4. Numerical examples

4.1. Model setup 1

For a first proof of concept a cylindrical model was prepared for simulation. The cylinder represents a column of seawater with a diameter of d = 0.5 m and a height of h = 1.0 m. The lateral surface is fixed in normal direction for displacements $\mathbf{u}_\mathrm{I}$ and closed for heat flux $\mathbf{q}$. The bottom surface allows heat transport. The whole cylinder is initiated with a temperature of θ = 272.15 K (−1.0 °C), a fixed bulk salinity of S^{bulk} = 35 PSU (PSU ≙ Practical Salinity Unit, equivalent to g/kg) and an initial volume fraction of ice of $\mathrm{n}^\mathbf{I}$ = 0.1 [−]. To start the simulation of the freezing process, four nodes in the middle of the top surface (marked in red) are impinged with a temperature decrease of $\Delta\theta$ = −10 K, see Fig. 7. The IBVP is chosen to consider a realistic physical condition, where a domain of seawater starts freezing from top due to lower atmospheric temperature. However, to observe the evolution of temperature also in the radial directions, the entire top surface is not prescribed with a Dirichlet boundary condition in this case.

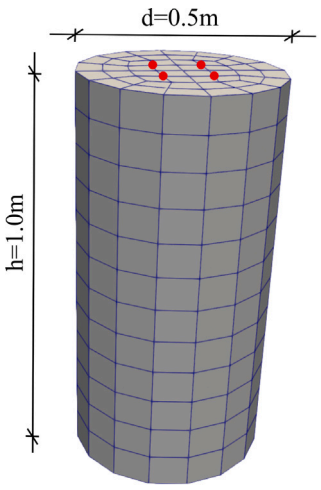

Fig. 7. Geometry and dimensions of initial boundary value problem (IBVP) setup 1. Red marked nodes are used to denote temperature decrease.

A total freezing time of 40 h was simulated, which was conducted with time increments of $\mathrm{d}t$ = 10 s using the parameters given in Table 1. Fig. 8 shows the spatial and temporal temperature propagation with lateral and vertical cooling of the water column.

In addition to that, Fig. 9 plots the spatial and temporal development of the volume fraction of ice $\mathrm{n}^\mathbf{I}$ during the simulation. The ice initially spreads also in the horizontal direction, and after reaching the lateral limits of the model ice grows vertically and the column freezes over, which can be well seen following the solidification front (yellow-green area).

Figs. 10(a) and 10(b) show the evolution of temperature and brine salinity over height at different time steps of the simulation, respectively at t = {t_0, 16 h, 40 h}. In the model the brine salinity S^{br} is implemented as a function of temperature, cf. Eq. (40). This equation represents the physical circumstances that only the freshwater part of sea water freezes to ice and the salt present is expelled to the liquid channels and pockets, which leads to the highly concentrated brine. During the simulation the salt content in the liquid accumulates to 150 PSU in the maximum, which yield from a volume fraction of ice $\mathrm{n}^\mathbf{I}$ = 0.4 at around θ = 262 K. This is in very good comparison to literature values, e.g. Fig. 6 in Vancoppenolle et al. (2010), where a temperature drop of roughly $\Delta\theta$ = −8 K yielding to a salinity of 140 PSU. Additionally, a least-square curve fit to data measurements between brine salinity and ice temperature, where a temperature of −10° C corresponds to 140 PSU is also discussed in Cox and Weeks (1986). Freezing of ice results in the non-linear distribution of the volume fractions of ice $\mathrm{n}^\mathbf{I}$ over the height, see Fig. 10(c). Starting with straight distributions from top to bottom, it adjusts to the curved course around 20 cm below the top surface. In that area the heat flux distributes in lateral and vertical direction. As soon as the boundaries

Table 1
Material parameter for BVP.

Material parameter	Liquid	Ice	Mixture
thermal conductivity [W/mK]	0.5 (Sharqawy et al., 2010)	2.2 (Kraitzman et al., 2024)	
specific heat capacity [J/kgK]	4180 (Lide, 2003)	2200 (Haynes, 2014)	
heat dilatation coefficient [K^{-1}]		5×10^{-5} (Petrenko and Whitworth, 1999)	
intrinsic permeability [m^2]		1×10^{-13} (Fowler and Iverson, 2022)	
dynamic viscosity sea water [Ns/m^2]	1.8×10^{-5} (Nayar et al., 2016)		
factor phase transition [–]			10

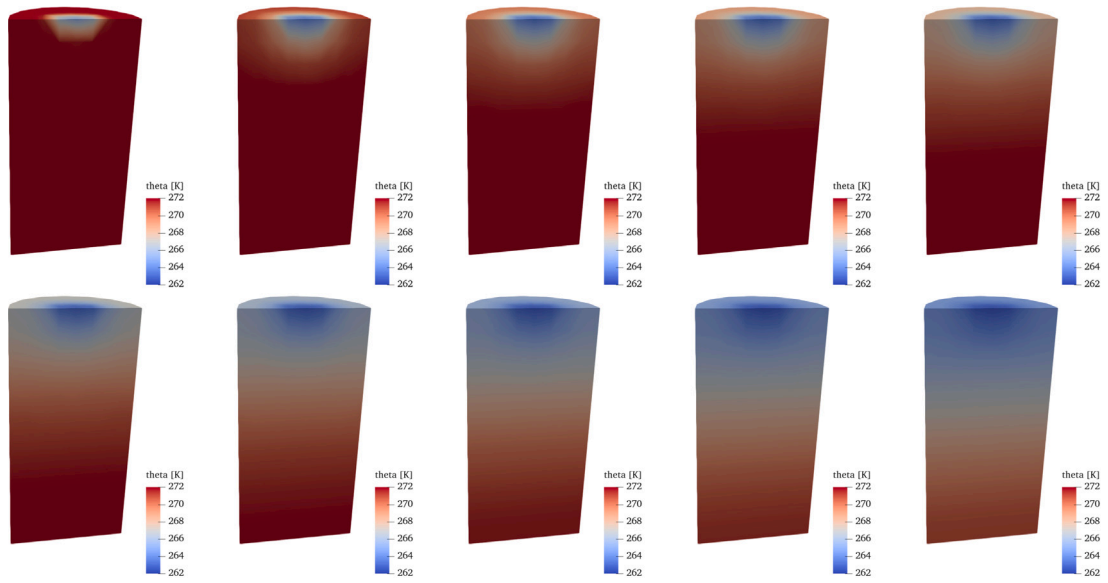

Fig. 8. Spatial development of temperature θ from simulation start to end with intermediate states.

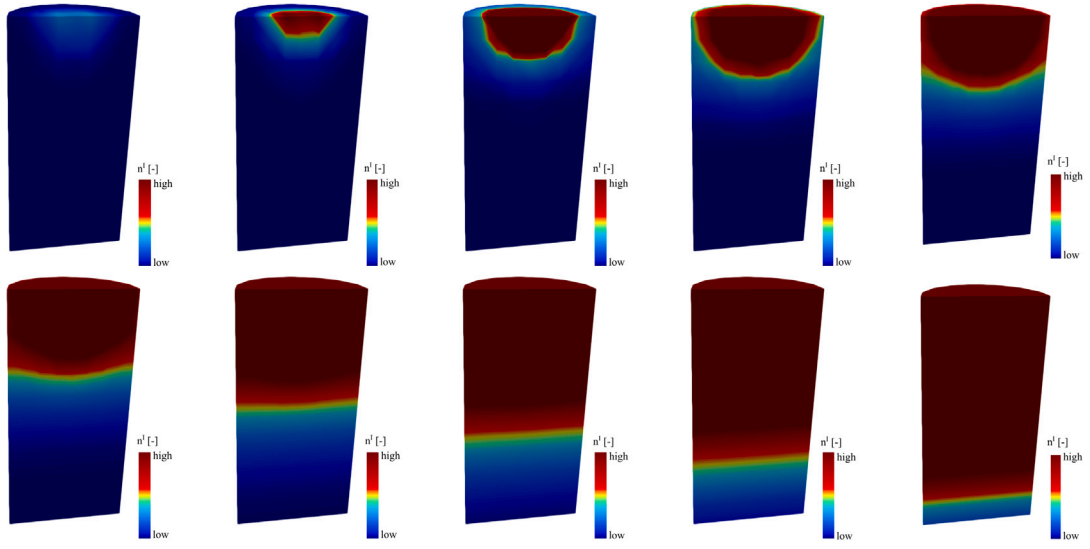

Fig. 9. Spatial development of ice-brine interface illustrated by the volume fraction n^I at different simulation time steps.

are reached, the heat only flows vertically causing the freezing of the column. As n^I increases, it can be observed in Fig. 10(d) that the growth rate of ice decreases. This behavior is attributed to the reduction in the temperature gradient over time, which affects the heat fluxes of ice and liquid in the Eq. (43).

To further evaluate how these variables evolve at various positions along the height over continuous time periods, Fig. 11 plots the development at the top, middle, and bottom layers of ice. The dynamics at different layers in the domain are quite distinct. While the upper layer starts below the freezing temperature, the middle and bottom layers only subsequently experience lower temperatures. It can be observed again that the ice fraction and growth rate follow opposite trends over time to preserve the saturation condition between the phases, as given in Eq. (3). In addition, distinct thermo-solutal coupling is evident. The ice fraction increases while the ice growth rate progressively declines due to latent heat release, reducing the local driving force for

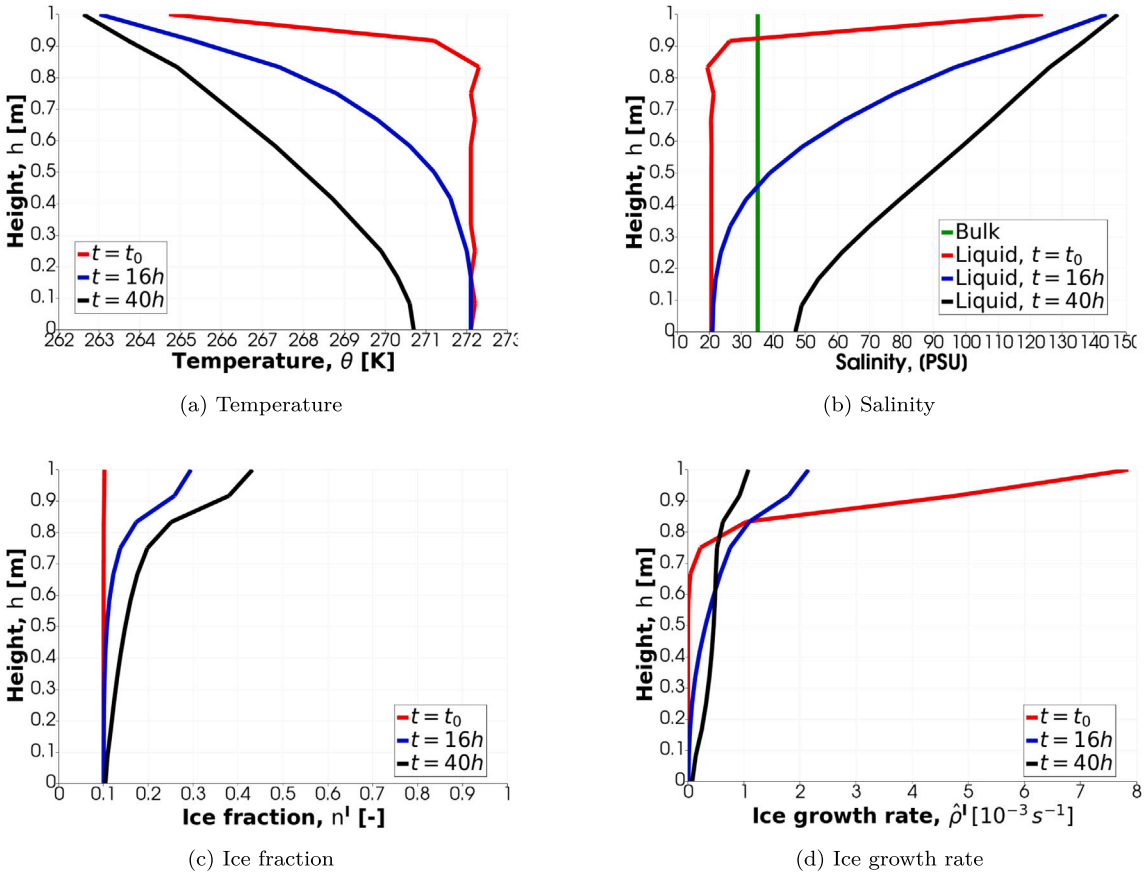

(a) Temperature (b) Salinity

(c) Ice fraction (d) Ice growth rate

Fig. 10. Evolution of key variables along height.

solidification. Rapid cooling at the top initiates early ice formation and brine rejection, sharply increasing the local salinity, whereas the middle and bottom layers exhibit delayed thermal and solutal responses. This leads to a vertically stratified structure, characterized by colder, fresher ice near the top and warmer, more saline liquid near the bottom. Over time, temperature and salinity gradients intensify, substantially influencing phase change dynamics and solute redistribution within the system.

The layers also experience varied behavior along the radial direction. Fig. 12 shows the profiles of various parameters at the end of the simulation. It is observed that, although there is a clear difference in the temperature and salinity profiles, the ice fraction and growth rates behave differently. At increasing vertical positions h, the system exhibits a pronounced phase change phenomena, characterized by elevated ice fractions $\mathrm{n}^{\mathbf{I}}$, higher ice growth rates $\hat{\rho}^{\mathbf{I}}$, increased salinity levels, and reduced temperature. The radial distributions of $\mathrm{n}^{\mathbf{I}}$ and $\hat{\rho}^{\mathbf{I}}$ display symmetry about the centerline ($\mathrm{x} = 0$), with maximum values at the center and monotonic decreases towards the lateral boundaries, indicative of a spatially non-uniform but radially symmetric solidification front $\mathbf{n}_{\Gamma}$. Salinity profiles demonstrate an overall increase with height while remaining nearly invariant along the radial coordinate. At the same time, temperature fields exhibit pronounced central minima corresponding to regions of maximal ice formation, highlighting the thermodynamic coupling between latent heat release and solute redistribution. These observations collectively suggest that the interplay between thermal gradients, solute segregation, and phase kinetics leads to a stratified structure, with stronger freezing, salt accumulation, and thermal gradients predominantly occurring at upper layers and near the domain center.

Pointing towards the "Rule of fives" (Golden et al., 1998, 2007), and more recently, also its improvement (Maus et al., 2021; Maus, 2025), disconnected pores only occur when the ice volume fraction is higher than 95% ($\mathrm{n}^{\mathbf{I}} > 0.95$). Therefore, in the present simulation setup, liquid fraction is still sufficiently high to have connected pores within the solid ice matrix. It must also be noted here, that the simulation experiment is carried in a non-equilibrium setting, meaning that empirical relations of equilibrium states, such as those presented in Cox and Weeks (1983), cannot be directly utilized to validate the non-equilibrium sea ice evolution states that the model produces.

4.2. Model setup 2

A second BVP was setup to further evaluate the growth of sea ice. In this case, instead of the previously chosen cylindrical column, a cubical domain was set up with a Dirichlet boundary condition on temperature at the top surface to imitate atmospheric low-temperature conditions compared to ocean temperature. Fig. 13 shows the schematic of the BVP. Radial effects, although important, have been neglected in this simulation setup.

Apart from the previously investigated results, in the setup, sensitivity to prescription of $\mathrm{n}^{\mathbf{I}}_0$ and θ is studied to understand if these have an effect on the results. Fig. 14 displays a parametric analysis of the vertically resolved ice fraction $\mathrm{n}^{\mathbf{I}}$ as a function of both initial ice content $\mathrm{n}^{\mathbf{I}}_0$ and temperature θ, capturing the interplay between compositional and thermal controls on sea ice formation. At all temperatures, higher values of $\mathrm{n}^{\mathbf{I}}_0$ yield uniformly greater ice fractions throughout the vertical column, indicating that the initial brine composition (eq. (40)), directly governs the maximum attainable ice volume. As θ decreases from $-2^{\circ}\,C$ to $-12^{\circ}\,C$, the profiles become increasingly non-linear, with ice accumulating more rapidly near the surface, leading to higher vertical gradients of $\mathrm{n}^{\mathbf{I}}$. This suggests enhanced freezing rates and sharper thermal stratification at colder temperatures. Notably, the relative influence of temperature is more pronounced at lower $\mathrm{n}^{\mathbf{I}}_0$, where vertical growth is initially suppressed but responds more sensitively to cooling.

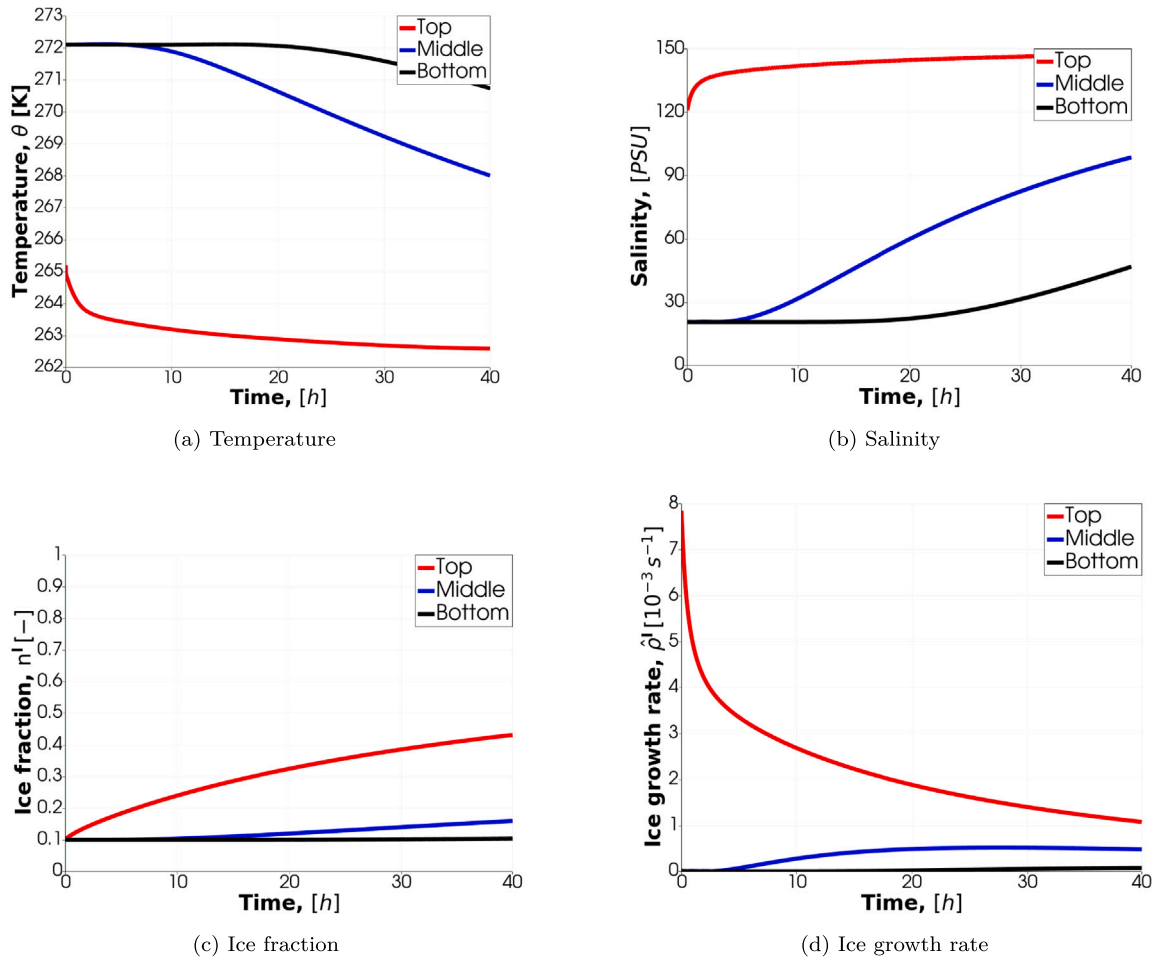

(a) Temperature (b) Salinity

(c) Ice fraction (d) Ice growth rate

Fig. 11. Evolution of key variables along height.

These trends imply that under colder conditions, sea ice structure becomes more vertically heterogeneous, and systems with lower initial ice fractions exhibit greater thermodynamic sensitivity.

To further investigate the effects of these parameters on freezing process, sea ice growth rate $\hat{\rho}^{\mathbf{I}}$ is in Fig. 15. It can be observed that a complex interplay between $n_0^{\mathbf{I}}$ and θ shape the vertical distribution of the ice growth rate $\hat{\rho}^{\mathbf{I}}$. At lower freezing conditions (e.g., $\theta = -2^{\circ}C$), growth rates are sharply peaked near the interface and diminish rapidly with depth, suggesting surface-dominated solidification. However, as temperature decreases, the growth rate profiles broaden and shift upward, indicating enhanced solidification across a larger vertical extent. Interestingly, the influence of $n_0^{\mathbf{I}}$ becomes increasingly nonlinear with cooling, meaning that, at low temperatures, small increments in $n_0^{\mathbf{I}}$ lead to disproportionately large increases in $\hat{\rho}^{\mathbf{I}}$, particularly in the upper half of the domain. This behavior reflects the coupling between thermodynamic forcing and microstructural feedbacks by means of ice fraction, where a greater initial ice fraction facilitates more rapid ice accumulation under stronger thermal gradients. The observed profile shapes highlight a transition from diffusion limited to thermodynamically enhanced growth regimes. Such vertical structuring of ice growth rate can be central to understanding microstructural morphology, and porosity evolution of sea ice.

4.3. Model setup 3

In this setup, further investigations are carried out by varying the boundary conditions. Fig. 16 shows the prescribed temperature BC to imitate seawater and atmospheric interfaces with sea ice. Contrary to Model 2 (Section 4.2), where seawater temperature was only prescribed as an initial condition in the entire domain except the top surface, in this model run, apart from the initial condition in the domain, the bottom surface is fixed at $\theta = -1.8°C$. This suggests that the possibility of free ice growth remains only within the domain and not at the upper and lower boundaries.

Figs. 17 and 18 show the development of the ice growth rate and volume fraction at $t = t_0, 16$ h, 40 h at $\theta_{top} = -10°C$ and $\theta_{bottom} = -1.8°C$. The sequence in Fig. 17 captures the dynamic evolution of the ice growth rate profiles over time for varying initial ice fractions $n_0^{\mathbf{I}}$. At the initial time $t = t_0$, growth rates are sharply localized near the interface, exhibiting peak values that correlate positively with $n_0^{\mathbf{I}}$, while the bulk remains relatively inactive. By $t = 16$h, the growth front has penetrated deeper, and distinct vertical gradients emerge with higher $n_0^{\mathbf{I}}$ leading to faster upward propagation of the freezing front. At $t = 40$h, the growth rate becomes more spatially distributed, with profiles flattening in the lower half and steepening near the top. The upward shift of peak $\hat{\rho}^{\mathbf{I}}$ indicates a transition from interface-dominated (due to BCs) to volumetric (due to coupled field effects) growth. Notably, systems with higher $n_0^{\mathbf{I}}$ continue to exhibit stronger growth across the full vertical domain, confirming the persistent influence of composition on thermally driven solidification kinetics.

Following the trends of $\hat{\rho}^{\mathbf{I}}$, $n^{\mathbf{I}}$ also evolve along the height in different behaviors. At $t = t_0$, ice fractions reflect their respective $n_0^{\mathbf{I}}$ values, with nearly uniform vertical profiles due to homogeneous distribution as initial conditions. After 16 h, the profiles begin to evolve with increasing curvature, particularly for higher $n_0^{\mathbf{I}}$, where the accumulation is more pronounced near the interface. By $t = 40$h, the system exhibits

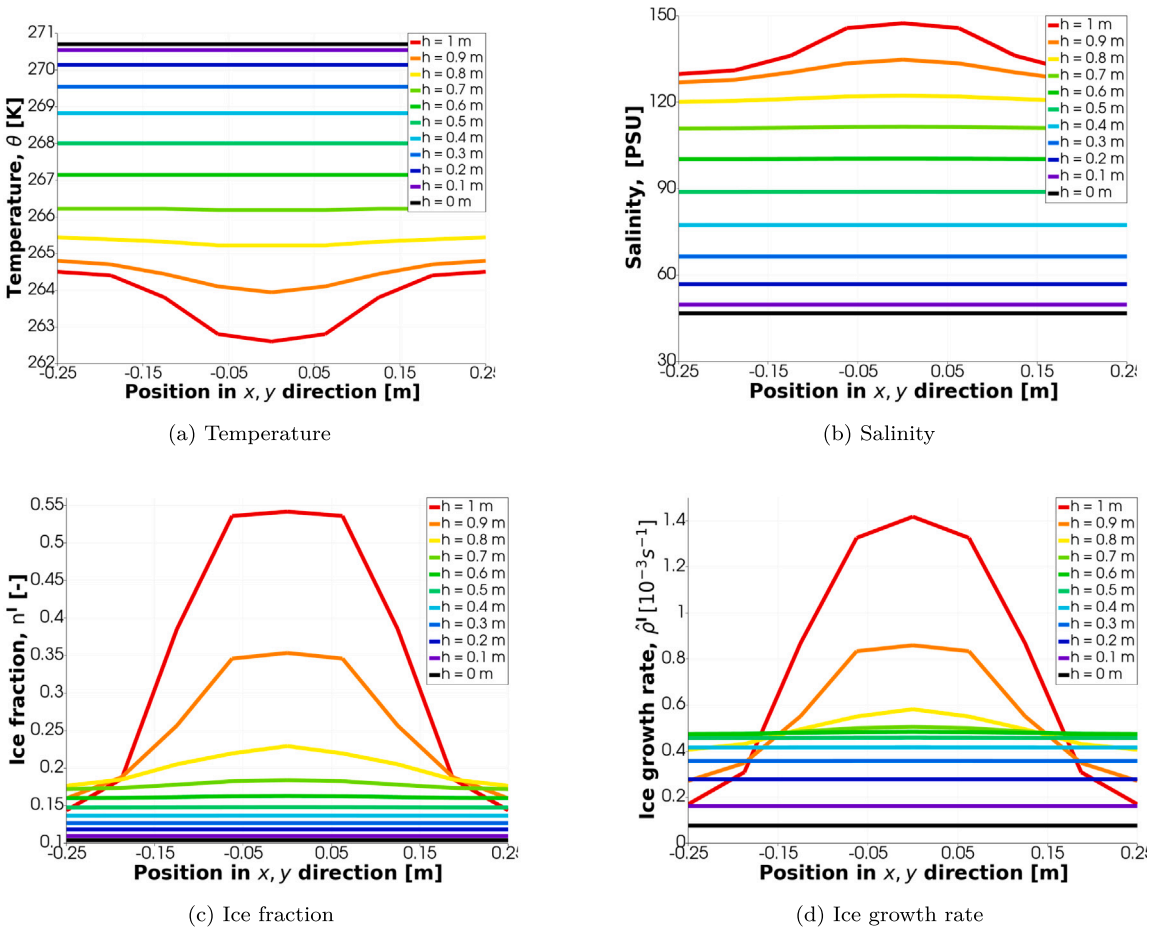

(a) Temperature (b) Salinity

(c) Ice fraction (d) Ice growth rate

Fig. 12. Developed variables at various layers.

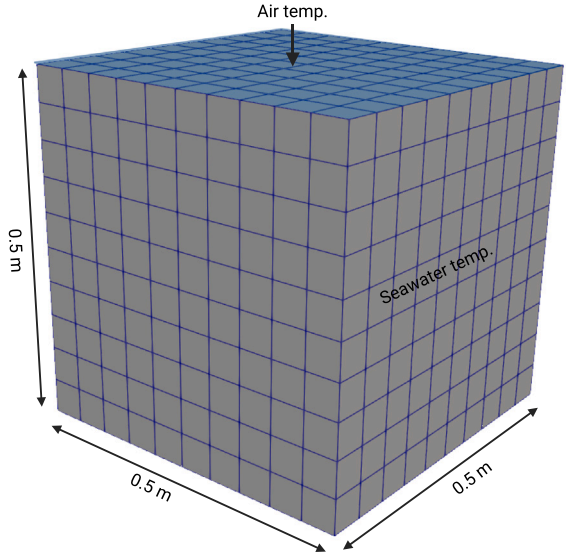

Fig. 13. Geometry and dimensions of initial boundary value problem (IBVP) setup 2. Blue surface on top is used to denote temperature decrease.

strong vertical variations where ice fractions increase with height, and differences between curves become more pronounced. This behavior highlights the non-uniform solidification front progression, with higher initial ice fractions promoting more rapid ice build-up near the colder boundary on the top. The time-resolved profiles illustrate how the interplay between thermal diffusion and phase transition kinetics leads to distribution of ice fraction.

Thus, through these sensitivity studies, it can be concluded that time, initial distribution of ice, and temperature values and boundary conditions can play a role in the behavior of sea ice growth.

The development of coupled salinity, temperature, ice growth rate and ice fraction profiles provides insight into the thermodynamic freezing of ocean water due to low temperature atmospheric conditions. Observations on depth dependent salinity and ice volume fraction from lab grown ice cores in controlled settings of temperature, and salt content can be a first approach to validate such simulations. Another approach could be to extract real sea ice cores (Notz et al., 2005), cut them into small discs at various heights and melt them. This would yield bulk salinity which can then directly be compared to this homogenization approach. However, the homogenized simulation and melted core salinity measurements will both be devoid of the true geometrical brine microstructure composition. Several other processes also influence the formation of sea ice and the associated desalination mechanisms, such as gravity drainage and flushing (Turner et al., 2013; Rees Jones and Grae Worster, 2014). TPM provides a modeling framework to couple with other multi-physical models like phase field solidification on the microscale. A more precise description of microscale desalination mechanisms will lead to more accurate behavior with the homogenized continua. This will, however, be a part of future work in this direction.

5. Conclusion

A continuum mechanical multi-phase and multi-component model for the description of freezing processes of seawater in the framework

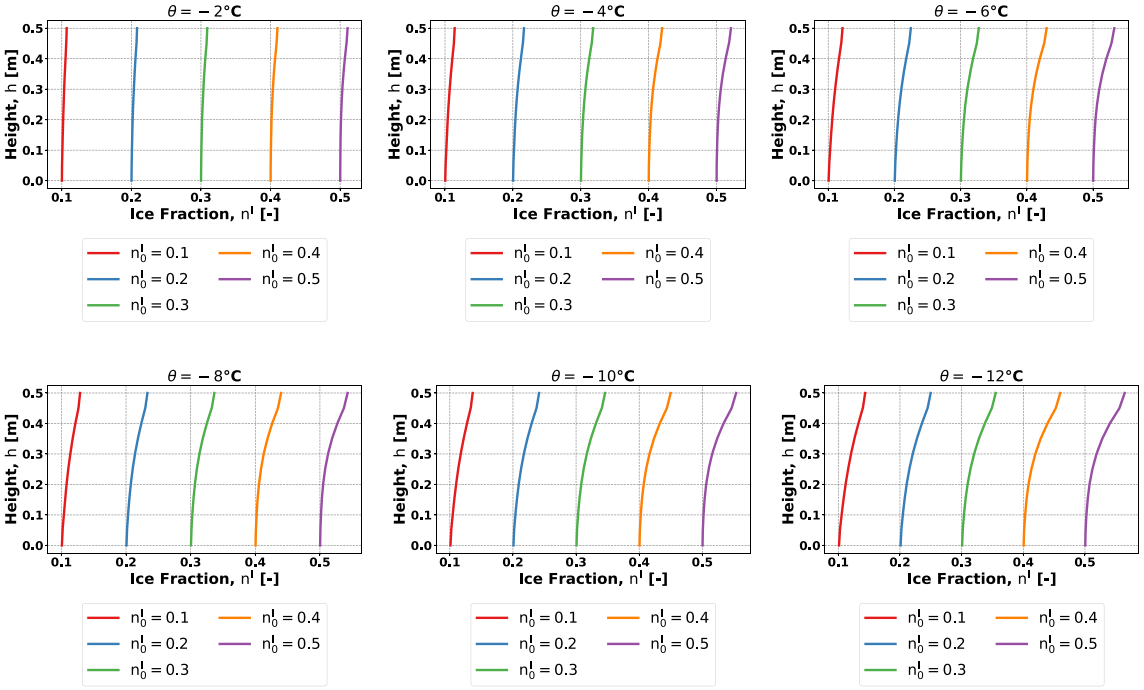

Fig. 14. Dependence of n^I on n_0^I and θ.

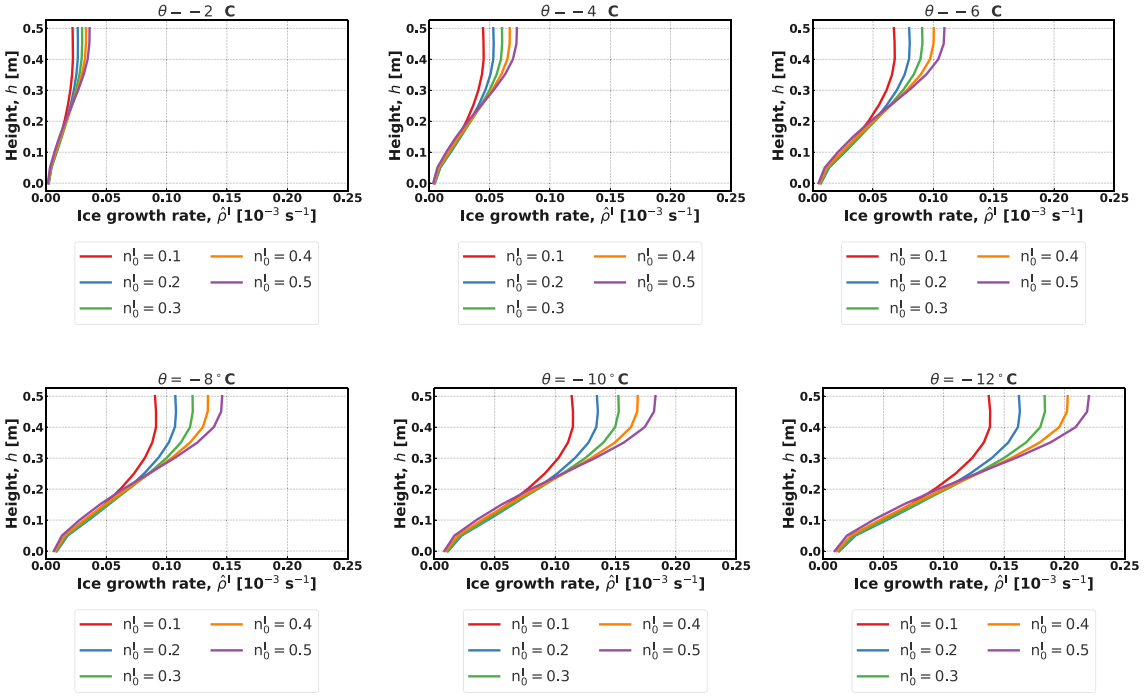

Fig. 15. Dependence of $\hat{\rho}^I$ on n_0^I and θ.

of extended Theory of Porous Media (eTPM) has been developed. Restrictions on conservative and dissipative quantities are derived by evaluating the Clausius–Duhem entropy inequality. The mass production term is formulated considering the heat fluxes and enthalpies of the solid and liquid phases, as well as the interfacial area. The brine salinity is modeled using temperature dependent third order polynomial function. Academic results through a variety of boundary conditions are presented and discussed in detail showing the utility of eTPM as an effective framework for modeling multiphasic and multi-component porous structure of sea ice. Sensitivity studies of the key factors are also performed and discussed to shed light upon their influence on the growth of sea ice. The developed model is quite general in its present state, and can also be utilized to model specific types of sea ice and also cater to the regional variations with different boundary

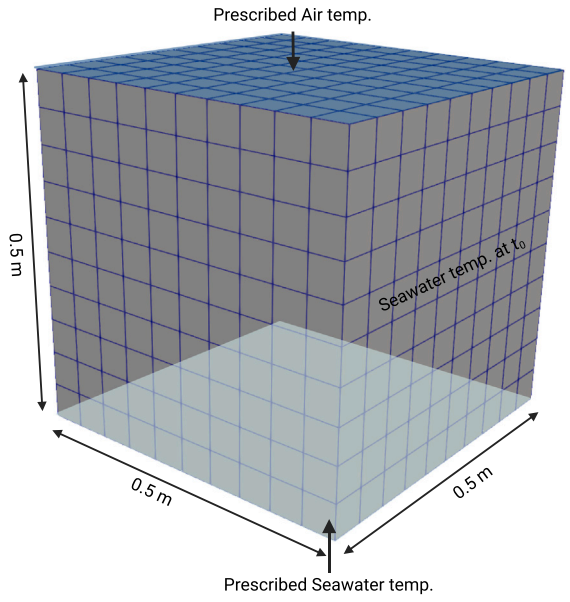

Fig. 16. Geometry and dimensions of initial boundary value problem (IBVP) setup 3. Blue surface on top is used to denote temperature decrease and green surface at the bottom specifies seawater temperature.

conditions and input parameters. In the future, the model will be coupled to the microscale brine channel and pore formation model presented in Morawetz et al. (2017), using phase field modeling and upscaling the pore size property to the continuum scale.

CRediT authorship contribution statement

Raghav Pathak: Writing – review & editing, Writing – original draft, Software, Investigation, Formal analysis, Data curation. **Seyed Morteza Seyedpour:** Writing – review & editing, Writing – original draft, Supervision, Methodology, Formal analysis, Conceptualization. **Bernd Kutschan:** Formal analysis. **Andrea Thom:** Conceptualization. **Silke Thoms:** Methodology, Funding acquisition, Formal analysis. **Tim Ricken:** Methodology, Funding acquisition.

Declaration of competing interest

The authors declare that they have no known competing financial interests or personal relationships that could have appeared to influence the work reported in this paper.

Acknowledgments

This work was supported by the Deutsche Forschungsgemeinschaft (DFG), Germany in the framework of the priority program SPP 1158 "Antarctic Research with comparative investigations in Arctic ice areas" by the following grant 463296570 (Priority Programme SPP 1158, Antarctica). T.R. further thanks the Deutsche Forschungsgemeinschaft (DFG, German Research Foundation), Germany for supporting this work via the following projects: 312860381 (Priority Program SPP 1886, Subproject 12); 390740016 (Germany's Excellence Strategy EXC 2075/1); 436883643 (Research Unit Programme FOR 5151 (QuaLiPerF), Project P7); 327154368 (SFB 1313 Project C03 Vertebroplasty); 504766766 (Project Hybrid MOR); 465194077 (Priority Programme SPP 2311, Project SimLivA). TR is further supported by the Federal Ministry of Education and Research (BMBF, Germany) within ATLAS by grant number 031L0304A. RP is supported by the Add-on Fellowship of the Joachim Herz Foundation, Germany.

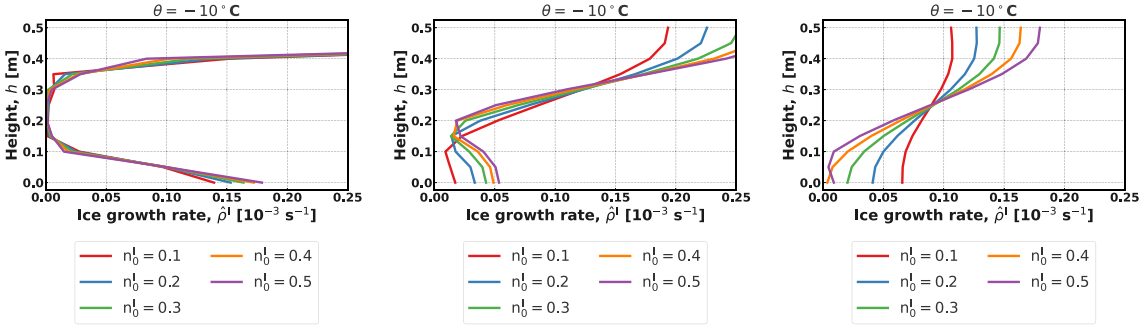

(a) t = t_0 (b) t = 16h (c) t = 40h

Fig. 17. Dependence of $\hat{\rho}^{I}$ on n_0^I at various times.

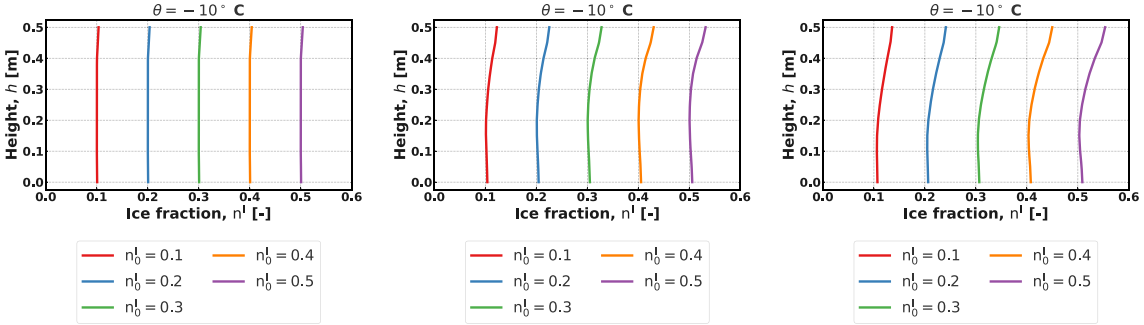

(a) t = t_0 (b) t = 16h (c) t = 40h

Fig. 18. Dependence of n^I on n_0^I at various times.

Data availability

Data will be made available on request.

References

Åström, J., Haapala, J., Polojärvi, A., 2023. A large-scale high-resolution numerical model for sea-ice fragmentation dynamics. Cryosphere Discuss. 2023, 1–16. http://dx.doi.org/10.5194/tc-2023-97, URL https://tc.copernicus.org/preprints/tc-2023-97/.

Babko, O., Rothrock, D.A., Maykut, G.A., 2002. Role of rafting in the mechanical redistribution of sea ice thickness. J. Geophys. Res. (Oceans) 107 (C8), 3113. http://dx.doi.org/10.1029/1999JC000190.

Bluhm, J., Bloßfeld, W., Ricken, T., 2014. Energetic effects during phase transition under freezing-thawing load in porous media - a continuum multiphase description and FE-simulation: Energetic effects during phase transition under freezing-thawing load in porous media. Z. Angew. Math. Mech. 94 (7–8), 586–608.

Bowen, R.M., 1967. Toward a thermodynamics and mechanics of mixtures. Arch. Ration. Mech. Anal. 24 (5), 370–403.

Bowen, R.M., 1969. The thermochemistry of a reacting mixture of elastic materials with diffusion. Arch. Ration. Mech. Anal. 34, 97–127. http://dx.doi.org/10.1007/BF00247461.

Bowen, R.M., 1976. Theory of mixtures. Contin. Phys. III, 1–127.

Coleman, B.D., Noll, W., 1963. The thermodynamics of elastic materials with heat conduction and viscosity. Arch. Ration. Mech. Anal. 13 (1), 167–178.

Cox, G.F.N., Weeks, W.F., 1983. Equations for determining the gas and brine volumes in sea-ice samples. J. Glaciol. 29 (102), 306–316. http://dx.doi.org/10.3189/S0022143000008364.

Cox, G., Weeks, W., 1986. Changes in the salinity and porosity of sea-ice samples during shipping and storage. J. Glaciol. 32 (112), 371–375.

Danilov, S., Wang, Q., Timmermann, R., Iakovlev, N., Sidorenko, D., Kimmritz, M., Jung, T., Schröter, J., 2015. Finite-element sea ice model (FESIM), version 2. Geosci. Model. Dev. 8 (6), 1747–1761. http://dx.doi.org/10.5194/gmd-8-1747-2015, URL https://gmd.copernicus.org/articles/8/1747/2015/.

De Boer, R., 1996. Highlights in the historical development of the porous media theory: Toward a consistent macroscopic theory. Appl. Mech. Rev. 49 (4), 201–262.

de Boer, R., Bluhm, J., 1999. Phase transitions in gas- and liquid-saturated porous solids. Transp. Porous Media 34, 249–267.

De Boer, R., Ehlers, W., 1988. A historical review of the formulation of porous media theories. Acta Mech. 74 (1–4), 1–8.

Deng, Q., Stechmann, S.N., Chen, N., 2024. Particle-continuum multiscale modeling of sea ice floes. Multiscale Model. Simul. 22 (1), 230–255. http://dx.doi.org/10.1137/23M155904X.

Doble, M., 2009. Simulating pancake and frazil ice growth in the Weddell Sea: A process model from freezing to consolidation. J. Geophys. Res. (Oceans) 114, http://dx.doi.org/10.1029/2008JC004935.

Drumheller, D.S., 1978. The theoretical treatment of a porous solid using a mixture theory. Int. J. Solids Struct. 14 (6), 441–456. http://dx.doi.org/10.1016/0020-7683(78)90009-4.

Ehlers, W., 2002. Foundations of multiphasic and porous materials. In: Ehlers, W., Bluhm, J. (Eds.), Porous Media. Springer Berlin Heidelberg, Berlin, Heidelberg, pp. 3–86.

Ehlers, W., 2014. Porous media in the light of history. In: Stein, E. (Ed.), The History of Theoretical, Material and Computational Mechanics - Mathematics Meets Mechanics and Engineering. vol. 1, Springer Berlin Heidelberg, Berlin, Heidelberg, pp. 211–227.

Ehlers, W., Haeberle, K., 2016. Interfacial mass transfer during gas–liquid phase change in deformable porous media with heat transfer. Transp. Porous Media 114 (2), 525–556.

Eicken, H., 1992. Salinity profiles of antarctic sea ice: Field data and model results. J. Geophys. Res.: Ocean. 97 (C10), 15545–15557.

Fang, Y., Wu, T., Hu, A., Chu, M., 2022. A modified thermodynamic sea ice model and its application. Ocean. Model. 178, 102096. http://dx.doi.org/10.1016/j.ocemod.2022.102096, URL https://www.sciencedirect.com/science/article/pii/S1463500322001123.

Fourier, J.B.J., 1822. Théorie analytique de la chaleur. F. Didot.

Fowler, J.R., Iverson, N.R., 2022. A permeameter for temperate ice: first results on permeability sensitivity to grain size. J. Glaciol. 68 (270), 705–713. http://dx.doi.org/10.1017/jog.2022.12.

Fu, D., Liu, B., Qi, Y., Yu, G., Huang, H., Qu, L., 2021. Multiscale variations in Arctic sea ice motion and links to atmospheric and oceanic conditions. Cryosphere 15 (8), 3797–3811. http://dx.doi.org/10.5194/tc-15-3797-2021, URL https://tc.copernicus.org/articles/15/3797/2021/.

Golden, K.M., Ackley, S.F., Lytle, V.I., 1998. The percolation phase transition in sea ice. Science 282 (5397), 2238–2241. http://dx.doi.org/10.1126/science.282.5397.2238.

Golden, K.M., Eicken, H., Heaton, A.L., Miner, J., Pringle, D.J., Zhu, J., 2007. Thermal evolution of permeability and microstructure in sea ice. Geophys. Res. Lett. 34 (16), http://dx.doi.org/10.1029/2007GL030447.

Griewank, P.J., Notz, D., 2013. Insights into brine dynamics and sea ice desalination from a 1-D model study of gravity drainage. J. Geophys. Res. C: Ocean. 118, 3370–3386.

Hassanizadeh, M., Gray, W.G., 1979a. General conservation equations for multi-phase systems: 1. Averaging procedure. Adv. Water Resour. 2, 131–144. http://dx.doi.org/10.1016/0309-1708(79)90025-3.

Hassanizadeh, M., Gray, W.G., 1979b. General conservation equations for multi-phase systems: 2. Mass, momenta, energy, and entropy equations. Adv. Water Resour. 2, 191–203. http://dx.doi.org/10.1016/0309-1708(79)90035-6.

Haynes, W.M. (Ed.), 2014. CRC Handbook of Chemistry and Physics, nintyfifth ed. CRC Press, http://dx.doi.org/10.1201/b17118.

Henning, C., Moj, L., Ricken, T., 2016. A ternary phase bi-scale FE-model for diffusion-driven dendritic alloy solidification processes. PAMM 16 (1), 449–450. http://dx.doi.org/10.1002/pamm.201610213.

Heorton, H.D.B.S., Radia, N., Feltham, D.L., 2017. A model of sea ice formation in leads and polynyas. J. Phys. Oceanogr. 47 (7), 1701–1718. http://dx.doi.org/10.1175/JPO-D-16-0224.1, URL https://journals.ametsoc.org/view/journals/phoc/47/7/jpo-d-16-0224.1.xml.

Hunke, E., Lipscomb, W., Jones, P., Turner, A., Jeffery, N., Elliott, S., 2017. CICE, the Los Alamos sea ice model, version 00. URL https://www.osti.gov//servlets/purl/1364126.

Kraitzman, N., Hardenbrook, R., Dinh, H., Murphy, N.B., Cherkaev, E., Zhu, J., Golden, K.M., 2024. Homogenization for convection-enhanced thermal transport in sea ice. Proc. R. Soc. A: Math. Phys. Eng. Sci. 480 (2296), 20230747. http://dx.doi.org/10.1098/rspa.2023.0747.

Kutschan, B., Morawetz, K., Gemming, S., 2010. Modeling the morphogenesis of brine channels in sea ice. Phys. Rev. E 81 (3), 036106. http://dx.doi.org/10.1103/PhysRevE.81.036106, URL https://link.aps.org/doi/10.1103/PhysRevE.81.036106.

Kutschan, B., Morawetz, K., Thoms, S., 2014. Dynamical mechanism of antifreeze proteins to prevent ice growth. Phys. Rev. E 90 (2), 022711. http://dx.doi.org/10.1103/PhysRevE.90.022711, URL https://link.aps.org/doi/10.1103/PhysRevE.90.022711.

Kutschan, B., Thoms, S., Bayer?Giraldi, M., 2016. Thermal hysteresis of antifreeze proteins considering Fragilariopsis cylindrus. Algological Stud. 151–152 (1), 69–86. http://dx.doi.org/10.1127/algol_stud/2016/0252, URL http://dx.doi.org/10.1127/algol_stud/2016/0252.

Lambers, L., 2023. Multiscale and multiphase modeling and numerical simulation of function-perfusion processes in the liver. Univ. Stuttg. URL http://elib.uni-stuttgart.de/handle/11682/13061.

Leppäranta, M., 2009. Sea ice dynamics. In: Steele, J.H. (Ed.), Encyclopedia of Ocean Sciences (Second Edition), second ed. Academic Press, Oxford, pp. 159–169. http://dx.doi.org/10.1016/B978-012374473-9.00640-8, URL https://www.sciencedirect.com/science/article/pii/B9780123744739006408.

Lewis, R.W., Schrefler, B.A., 1999. The Finite Element Method in the Static and Dynamic Deformation and Consolidation of Porous Media. John Wiley & Sons, Chinchester.

Lide, D.R. (Ed.), 2003. CRC Handbook of Chemistry and Physics, eightyfourth ed. CRC Press, http://dx.doi.org/10.1201/b17118.

Lieblappen, R.M., Kumar, D.D., Pauls, S.D., Obbard, R.W., 2018. A network model for characterizing brine channels in sea ice. Cryosphere 12 (3), 1013–1026. http://dx.doi.org/10.5194/tc-12-1013-2018, URL https://tc.copernicus.org/articles/12/1013/2018/.

Maus, S., 2025. Growth rate dependence of the permeability and percolation threshold of young sea ice. Faraday Discuss. http://dx.doi.org/10.1039/D4FD00172A, URL http://dx.doi.org/10.1039/D4FD00172A.

Maus, S., Schneebeli, M., Wiegmann, A., 2021. An X-ray micro-tomographic study of the pore space, permeability and percolation threshold of young sea ice. Cryosphere 15 (8), 4047–4072. http://dx.doi.org/10.5194/tc-15-4047-2021, URL https://tc.copernicus.org/articles/15/4047/2021/.

McDonald, A., 2018. Impacts of Rapid Regional Warming on Summer Sea Ice Extent at Wordie Bay, Western Antarctic Peninsula and Subsequent Impacts on the Earth System (Ph.D. thesis). The Open University.

McFarlane, V., Loewen, M., Hicks, F., 2015. Measurements of the evolution of frazil ice particle size distributions. Cold Reg. Sci. & Technol. 120, 45–55. http://dx.doi.org/10.1016/j.coldregions.2015.09.001, URL https://www.sciencedirect.com/science/article/pii/S0165232X1500186X.

Moj, L., 2017. A two-scale, two-phase model for the numerical simulation of thermal driven solidification processes during casting and forming of metallic materials. In: Berichte aus dem Bauwesen, Shaker Verlag, Aachen.

Moj, L., Foppe, M., Deike, R., Ricken, T., 2017. Micro-macro modelling of steel solidification: A continuum mechanical, bi-phasic, two-scale model including thermal driven phase transition: A continuum mechanical, bi-phasic, two-scale model including thermal driven phase transition. GAMM–Mitteilungen 40 (2), 125–137. http://dx.doi.org/10.1002/gamm.201720004.

Morawetz, K., Thoms, S., Kutschan, B., 2017. Formation of brine channels in sea ice. Eur. Phys. J. E 40 (3), 25. http://dx.doi.org/10.1140/epje/i2017-11512-x, URL http://link.springer.com/10.1140/epje/i2017-11512-x.

Nayar, K.G., Sharqawy, M.H., Banchik, L.D., V, J.H.L., 2016. Thermophysical properties of seawater: A review and new correlations that include pressure dependence. Desalination 390, 1–24. http://dx.doi.org/10.1016/j.desal.2016.02.024.

Nose, T., Waseda, T., Kodaira, T., Inoue, J., 2021. On the coagulated pancake ice formation: Observation in the refreezing Chukchi Sea and comparison to the Antarctic consolidated pancake ice. Polar Sci. 27, 100622, Arctic Challenge for Sustainability Project (ArCS) https://doi.org/10.1016/j.polar.2020.100622, URL https://www.sciencedirect.com/science/article/pii/S1873965220301456.

Notz, D., 2005. Thermodynamic and Fluid-Dynamical Processes in Sea Ice (Ph.D. thesis). University of Cambridge Cambridge.

Notz, D., Wettlaufer, J.S., Worster, M.G., 2005. A non-destructive method for measuring the salinity and solid fraction of growing sea ice in situ. J. Glaciol. 51 (172), 159–166. http://dx.doi.org/10.3189/172756505781829548.

Notz, D., Worster, M.G., 2009. Desalination processes of sea ice revisited. J. Geophys. Res.: Ocean. 114 (C5), http://dx.doi.org/10.1029/2008JC004885.

Passman, S., 1977. Mixtures of granular materials. Internat. J. Engrg. Sci. 15 (2), 117–129. http://dx.doi.org/10.1016/0020-7225(77)90027-1.

Pathak, R., Seyedpour, S.M., Kutschan, B., Thom, A., Thoms, S., Ricken, T., 2024. Modeling freezing and BioGeoChemical processes in Antarctic sea ice. PAMM 24 (2), e202400047. http://dx.doi.org/10.1002/pamm.202400047.

Pathak, R., Seyedpour, S.M., Kutschan, B., Thoms, S., Ricken, T., 2025. A coupled multiscale description of seasonal physical–BioGeoChemical dynamics in southern ocean marginal ice zone. Environ. Model. Softw. 185, 106270. http://dx.doi.org/10.1016/j.envsoft.2024.106270.

Paul, F., Schwarz, C., Audh, R., Bluhm, J., Johnson, S., MacHutchon, K., Mielke, T., Mishra, A., Rampai, T., Ricken, T., Schwarz, A., Skatulla, S., Thom, A., Verrinder, R., Schröder, J., Vichi, M., Lupascu, D., 2023. Sea ice mechanics. Comput. Methods Mater. Sci. 23 (3), 5–54. http://dx.doi.org/10.7494/cmms.

Petrenko, V.F., Whitworth, R.W., 1999. Physics of Ice. Oxford University Press.

Petrich, C., Eicken, H., 2016. Overview of sea ice growth and properties. In: Thomas, D.N. (Ed.), Sea Ice. John Wiley & Sons, Ltd, Chichester, UK, pp. 1–41.

Rees Jones, D.W., Grae Worster, M., 2014. A physically based parameterization of gravity drainage for sea-ice modeling. J. Geophys. Res. Ocean. 119, 5599–5621.

Ricken, T., 2002. Kapillarität in porösen Medien: theoretische Untersuchung und numerische Simulation: PhD-Thesis, first ed. Shaker.

Ricken, T., Bluhm, J., 2010a. Modeling fluid saturated porous media under frost attack. GAMM-Mitt. 33 (1), 40–56.

Ricken, T., Bluhm, J., 2010b. Remodeling and growth of living tissue: a multiphase theory. Arch. Appl. Mech. 80 (5), 453–465.

Ricken, T., de Boer, R., 2003. Multiphase flow in a capillary porous medium. Comput. Mater. Sci. 28 (3–4), 704–713. http://dx.doi.org/10.1016/j.commatsci.2003.08.032.

Ricken, T., Sindern, A., Bluhm, J., Widmann, R., Denecke, M., Gehrke, T., Schmidt, T., 2014. Concentration driven phase transitions in multiphase porous media with application to methane oxidation in landfill cover layers: Concentration driven phase transitions in multiphase porous media. Z. Angew. Math. Mech. 94 (7–8), 609–622.

Ricken, T., Thom, A., Gehrke, T., Denecke, M., Widmann, R., Schulte, M., Schmidt, T.C., 2020. Biological driven phase transitions in fully or partly saturated porous media: A multi-component FEM simulation based on the theory of porous media. In: Giovine, P., Mariano, P.M., Mortara, G. (Eds.), Views on Microstructures in Granular Materials. vol. 44, Springer International Publishing, Cham, pp. 157–183.

Schwarz, A., Bluhm, J., Schröder, J., 2020. Modeling of freezing processes of ice floes within the framework of the TPM. Acta Mech. 231 (8), 3099–3121.

Seyedpour, S., Janmaleki, M., Henning, C., Sanati-Nezhad, A., Ricken, T., 2019a. Contaminant transport in soil: A comparison of the theory of porous media approach with the microfluidic visualisation. Sci. Total Environ. 686, 1272–1281. http://dx.doi.org/10.1016/j.scitotenv.2019.05.095, URL https://www.sciencedirect.com/science/article/pii/S0048969719321138.

Seyedpour, S., Kirmizakis, P., Brennan, P., Doherty, R., Ricken, T., 2019b. Optimal remediation design and simulation of groundwater flow coupled to contaminant transport using genetic algorithm and radial point collocation method (RPCM). Sci. Total Environ. 669, 389–399. http://dx.doi.org/10.1016/j.scitotenv.2019.01.409, URL https://www.sciencedirect.com/science/article/pii/S0048969719304565.

Seyedpour, S.M., Thom, A., Ricken, T., 2023. Simulation of contaminant transport through the vadose zone: A continuum mechanical approach within the framework of the extended theory of porous media (eTPM). Water 15 (2), 343.

Sharqawy, M.H., V., J.H.L., Zubair, S.M., 2010. The thermophysical properties of seawater: A review of existing correlations and data. Desalination Water Treat. 16, 354–380, Version: Author's final manuscript.

Streffing, J., Sidorenko, D., Semmler, T., Zampieri, L., Scholz, P., Andrés-Martínez, M., Koldunov, N., Rackow, T., Kjellsson, J., Goessling, H., Athanase, M., Wang, Q., Hegewald, J., Sein, D.V., Mu, L., Fladrich, U., Barbi, D., Gierz, P., Danilov, S., Juricke, S., Lohmann, G., Jung, T., 2022. AWI-CM3 coupled climate model: description and evaluation experiments for a prototype post-CMIP6 model. Geosci. Model. Dev. 15 (16), 6399–6427. http://dx.doi.org/10.5194/gmd-15-6399-2022, URL https://gmd.copernicus.org/articles/15/6399/2022/.

Suditsch, M., Lambers, L., Ricken, T., Wagner, A., 2021. Application of a continuum-mechanical tumour model to brain tissue. PAMM 21 (1), e202100204. http://dx.doi.org/10.1002/pamm.202100204.

Taylor, R.L., 2014. FEAP - Finite Element Analysis Program. University of California, Berkeley, URL http://www.ce.berkeley/feap.

Tedesco, L., Vichi, M., 2014. Sea ice biogeochemistry: A guide for modellers. In: Dias, J.a.M. (Ed.), PLoS One 9 (2), e89217.

Terzaghi, K., 1943. Theoretical Soil Mechanics, first ed. Wiley.

Thom, A., 2022. Theory and Model Implementation of Gaseous Transport and Reaction Processes in Porous Media Applied to Methane Oxidation in Landfill Cover Layers (Ph.D. thesis). University of Stuttgart.

Truesdell, C., 1984. Rational Thermodynamics. Springer New York, New York, NY.

Turner, A.K., Hunke, E.C., Bitz, C.M., 2013. Two modes of sea-ice gravity drainage: A parameterization for large-scale modeling. J. Geophys. Res.: Ocean. 118, 2279–2294. http://dx.doi.org/10.1002/jgrc.20171.

Vancoppenolle, M., Goosse, H., De Montety, A., Fichefet, T., Tremblay, B., Tison, J.-L., 2010. Modeling brine and nutrient dynamics in Antarctic sea ice: The case of dissolved silica. J. Geophys. Res. 115 (C2), C02005.

Vancoppenolle, M., Madec, G., Thomas, M., McDougall, T.J., 2019. Thermodynamics of sea ice phase composition revisited. J. Geophys. Res.: Ocean. 124 (1), 615–634. http://dx.doi.org/10.1029/2018JC014611.

Vancoppenolle, M., Tedesco, L., 2017. Numerical models of sea ice biogeochemistry. In: Thomas, D.N. (Ed.), Sea Ice. Wiley, Chichester, UK, pp. 492–515.

Weeks, W.F., Ackley, S.F., 1986. The growth, structure, and properties of sea ice. In: The Geophysics of Sea Ice. Springer US, Boston, MA, pp. 9–164. http://dx.doi.org/10.1007/978-1-4899-5352-0_2.

Weiss, J., Dansereau, V., 2017. Linking scales in sea ice mechanics. Philos. Trans. R. Soc. A: Math. Phys. Eng. Sci. 375 (2086), 20150352. http://dx.doi.org/10.1098/rsta.2015.0352.

Worster, M.G., Rees Jones, D.W., 2015. Sea-ice thermodynamics and brine drainage. Philos. Trans. R. Soc. A: Math. Phys. Eng. Sci. 373 (2045), 20140166.